A microfluidics-assisted photopolymerization method for high-resolution multimaterial 3D printing

Victor Fournié, Bastien Venzac, Emmanuelle Trevisiol, Julie Foncy, Julien Roul, Sandrine Assié-Souleille, Mélanie Escudero, Pierre Joseph, Arnaud Reitz, Laurent Malaquin

A microfluidics-assisted photopolymerization method for high-resolution multimaterial 3D printing

Victor Fournié[a,c] (vfournie@laas.fr), Bastien Venzac[a] (bvenzac@laas.fr), Emmanuelle Trevisiol[b] (emmanuelle.trevisiol@insa-toulouse.fr), Julie Foncy[a] (jfoncy@laas.fr), Julien Roul[a] (jroul@laas.fr), Sandrine Assie-Souleille[a] (sassie@laas.fr), Mélanie Escudero[d] (melanie.escudero@inserm.fr), Pierre Joseph[a] (pierre.joseph@laas.fr), Arnaud Reitz[c] (arnaud.reitz@fluigent.com), Laurent Malaquin[a] (lmalaqui@laas.fr)

[a] Laboratoire d'analyse et d'architecture des systèmes-CNRS, Toulouse, 31400, FRANCE
[b] Toulouse Biotechnology Institute-INSA-CNRS, Toulouse, 31400, FRANCE
[c] Fluigent SA , Kremlin-bicètre, 94270, FRANCE
[d] RESTORE Research Center, Université de Toulouse, INSERM 1301, CNRS 5070, EFS, ENVT, 31100 Toulouse, France

Corresponding author: Victor Fournie (vfournie@laas.fr)

Abstract

3D printing and bioprinting are recognized as key technologies for the construction of complex micro-devices, micro-environments, and culture models. Thanks to their potential to produce precisely heterogeneous and 3D architectures, multimaterial printing methods, which enable the production of functional 3D structures integrating multiple materials, have attracted specific attention. Nevertheless, combining multimaterial and high-resolution printing is still a major challenge, and the available technologies do not provide simultaneously the resolution and multiplexing capabilities required to create heterogeneous 3D environments. In this work, we introduce the 3D-FlowPrint concept, which involves an opto-microfluidic printhead immersed in a liquid and moved above a surface. This technology combines the convenience of microfluidics in terms of the handling and delivery of small volumes of materials with the resolution provided by laser lithography. Delivered materials are hydrodynamically confined under the printhead owing to controlled aspiration of the injected material, ensuring a continuous supply of material and avoiding cross-contamination issues. Combining microfluidics with photo-polymerization provides unique advantages as it separates the polymerization process from the material delivery, permitting high-resolution polymerization (down to 10 µm) and multimaterial handling (switching time below 60 s). We present a first proof-of-concept using poly(ethylene glycol) diacrylate (PEGDA)-based hydrogels as a photosensitive material model, along with a detailed investigation of the influence of exposure parameters, printhead velocity, and hydrodynamic parameters on the fabrication of 2D and 3D heterogeneous structures. 3D-FlowPrint allows the creation of sub-millimetric to millimetric scale objects with multimaterial designs. A first validation was performed to show the potential of the approach in biology for the creation of engineered microenvironments for cell culture.

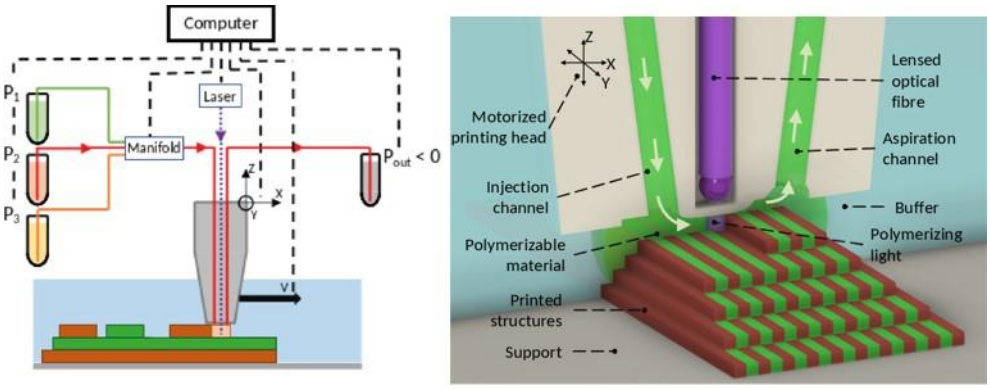

Keywords:

- Additive manufacturing
- Multimaterial 3D printing
- High-resolution 3D printing
- Photopolymerization
- Microfluidics

Abbreviations and variables

V: printhead velocity

Z_{gap}: gap between the substrate and the printhead, measured at the closest point under the PDMS dome in the polymerization area

φ_{in}, φ_{out}: Injection and aspiration flowrates

$R\varphi = \varphi_{out}/\varphi_{in}$: flowrate ratio

μ_{mat}, μ_{med}: dynamic viscosities of the injected material and of the medium respectively

HFC: Hydrodynamic flow confinement

Rr: Retrieval rate, defines the mass ratio between the injected and retrieved material when reaching steady state regime

1 Introduction

Additive manufacturing is the state-of-the-art for the fabrication of complex three-dimensional (3D) structures. Recent advances have enabled 3D printing of biocompatible materials, cells, and supporting components to create 3D scaffolds or 3D models of functional living tissues [1].

Typically, these models contain several cell types in close proximity (<100 µm) and at various densities encapsulated inside hydrogels having a large range of mechanical properties and biochemical compositions. The ability to print one construct with different hydrogels, each containing (or not) different cell types or the same cells at different densities with resolutions close to tens-of-micrometers is a key enabling feature for the creation of relevant models [2]–[6]. However, few concepts have managed to combine a simple method for multimaterial printing with such resolution. Traditional micro-extrusion [7] or inkjet printing [5] are well recognized as efficient techniques to create multimaterial structures, but they still present some issues in terms of resolution, mainly driven by the size of the extrusion system or the dimensions of the generated droplets. Laser-assisted techniques [8], [9] enable higher resolution, but the photopolymerization process usually takes place in a vat containing one single material, making it challenging to print multimaterial objects.

Photolithography-based methods have been widely investigated for additive manufacturing and bioprinting [10]. They show promise in terms of resolution as they allow the separation of the mass transport mechanism from structuration aspects and thus high resolutions at the sub-micrometer scale [11]. The development of multimaterial approaches combined with photolithography has naturally attracted huge interest in recent years. Compared with traditional extrusion printing, where cylindrical filaments of liquid or shear-thinning bioinks are physically deposited with a moving nozzle, stereolithography (SLA) [12], [13] uses controlled illumination to selectively photocrosslink liquid bioinks into solid features, offering superior spatial resolution to that of extrusion or inkjet printers. However, conventional SLA systems are almost exclusively designed to print hard plastic materials for non-biological applications and few offer multimaterial capability [6]. Combining the resolution of laser-based 3D printing methods with the capacity of printing heterogeneous structures starting from a material library has attracted huge interest in bioprinting, among other fields [14]. A straightforward and common approach is to perform sequential printing processes where the samples are moved into different vats to perform successive development and material immersion steps [15]–[17]. This gives rise to efficient but tedious manipulations that hinder the global printing throughput. From the perspective of developing more straightforward processes, Grigoryan et al. proposed a multi- material SLA bioprinter involving a motorized sled allowing nascent structures to interface with separate bioinks of variable chemical or cellular compositions [18]. This method has proven to be compatible with photoresists and hydrogel materials adapted to bioprinting. However, the authors acknowledged certain limitations of the printing system with respect to scale, resolution, automation, and material selection. Beyond the feature-size limitations inherent to projection SLA, the construction of large structures with complex internal heterogeneity would require numerous rinsing and material-change steps making this technique laborious. Peng et al have proposed in 2021 an interesting combination of micro-extrusion, for functional materials, and photolithography, for high speed and high resolution printing. However, limitation of both technics remain

The integration of fluidic control to ensure automated injection has attracted huge interest over the last few years. In 2018, Miri et al. developed a microfluidic chip with sequential injection allowing the printing of multimaterial structures [19]. A Z platform deforming a flexible PDMS membrane allowed the fabrication of 3D objects. Despite the ingenuity of the system, several drawbacks were presented, such as size limitations in the XY plane and the Z direction as well as stress on the PDMS membrane and the structure due to the movement of the Z platform. On a larger scale, Han et al. have proposed a micro-SLA method based on the integration of a microfluidic cell surrounding the sample that permits a fast and sequential injection of different materials with viscosities up to 58 mPa.s [20]. The authors have shown the injection of several material with fast switching times but relatively high flowrate of ~1 mL/s that could be detrimental for soft material applications. A similar concept was also successfully applied to multiphoton lithography in the work of Mayer et al. [21]. By optimization of the microfluidic circuitry, the authors demonstrated multimaterial capacity with a reduction of the swept volumes to 500 µL. However, due to specific constraints imposed by the objective, the geometry of the chamber limits the height of the printed samples to 100 µm. More recently, Lipkowitz et al. proposed an alternative approach that uses the active control of mass transport combined with continuous liquid interface printing [22]. This approach permits multimaterial injection and delivery in the exposure area to allow rapid printing of multiple different resins simultaneously at varying scales. However, this method relies on the integration of the fluidic injection channels directly in the fabricated structures and is subject to potential issues related to material recovery and subsequent contamination.

Several of these methods profit from the miniaturization of 3D printing concepts into microfluidic devices and present the possibility of reducing the volumes of liquid and providing better control and reproducibility of flowrates. Microfluidics provides parallelization and multiplexing capacities that are essential to mix and accurately tune the composition of the materials thanks to an integrated microfluidic circuitry. Skylar-Scott et al. demonstrated the integration of microfluidics in the printhead in the context of extrusion printing [23]. The authors reported the design and fabrication of voxelated matter using multimaterial multinozzle 3D (MM3D) printing. Simple or multi-photon approaches have also been reported for enclosed microfluidic devices for the fabrication of small (<1 mm) 3D objects or particles through continuous flow lithography [24], [25]. However, such methods impose a Z limitation on the objects between the two planes of the microfluidic chip, and this prevents or complicates the creation of 3D objects. Clearly, despite certain inherent limitations induced by either large material consumption, design limitations, or contamination issues, all these approaches demonstrate the opportunities provided by laser-assisted methods and/or fluidic systems

for multimaterial printing as they decouple mass transport and material delivery from the writing mechanism, i.e., photopolymerization.

Here, we propose the 3D-FlowPrint concept (Fig. 1, [26]), an original printhead design with hydrodynamic confinement that provides fast and efficient microfluidic injection in the printing area. The use of both aspiration and injection systems with controllable pressures allows efficient recovery of excess injected material in the printing area, thus limiting the risk of contamination in the surrounding media. From a conceptual point of view, this device borrows some of the aspects of the microfluidic probe concept first proposed by D. Juncker and E. Delamarche [27]–[29]. However, 3D-FlowPrint relies on a different design allowing the injection of viscous materials and the possibility to work at long distances (>500 µm) from a substrate. Furthermore, an optical fiber is integrated in the printhead to photopolymerize the material during material injection. Unlike most applications, the light does not cross the material container layer but is directly provided in the printhead close to the fluidic delivery system. To our knowledge, the integration of a light source within such a device to precisely photopolymerize hydrogels has not been reported. The combination of an open microfluidic device with integrated optics opens a new field of research for the 3D structuring of materials. Contrary to previous works, our approach provides the ability to control spatially the composition of the structures with multiple materials and enable the fabrication of multiscale 3D objects.

In this article, the printhead fabrication protocol, including its 3D SLA printing and assembly, is presented. We describe hydrodynamic aspects of the system, its optimization through Comsol simulations, and its operative regime. The in-flow photopolymerization is explained and analyzed. Finally, we present 3D pieces with precise evaluation of

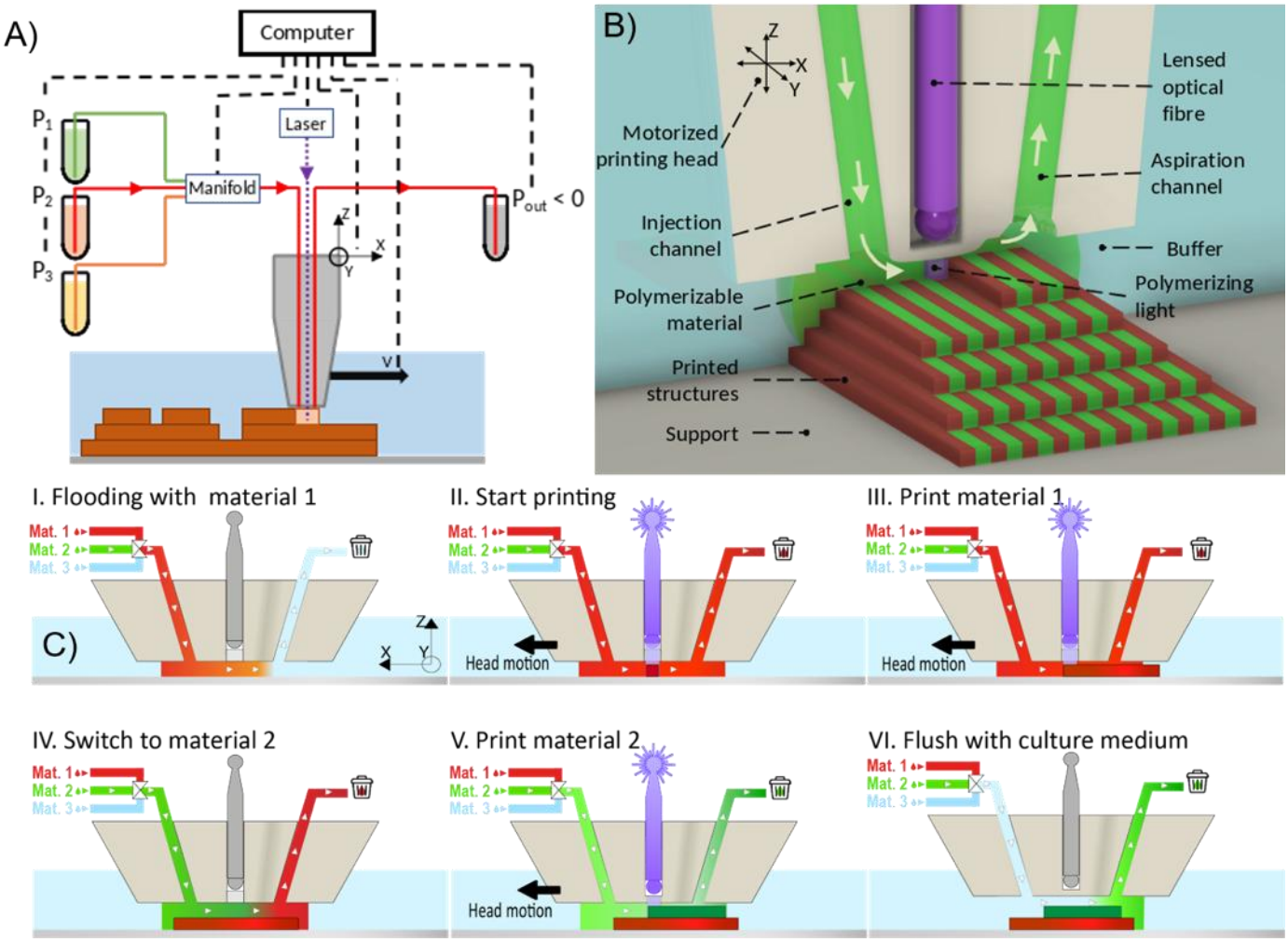

Figure 1. 3D Illustration of the 3D-FlowPrint concept. (A) Planar schematics showing the setup of the instrument (B) Schematic of the opto-fluidic processes with a XZ cross-section of the head. (C) Multimaterial printing workflow.

XYZ attributes as well as details of their multimaterial characteristics and their use in the study of spheroid/cell cultures on structured materials.

2 Materials and methods

2.1 Materials and chemicals

Poly-(ethylene glycol) diacrylate (PEGDA) Mw = 700 g/mol, lithium-2,4,6-trimethylbenzoylphosphinate (LAP), Rhodamine B, 3-methacryloxypropyltrimethoxysilane (MAPTMS), phosphate-buffered saline (PBS), polydimethylsiloxane (PDMS) Sylgard 184 (Dow Corning) were purchased from Sigma-Aldrich. Fluorescent carboxylate-modified particles (FluoSpheres™ D = 200 nm and Fluoro-Max™ D = 300 nm or D = 5 µm) were purchased from Thermo Fischer. Epotek 301 glue was purchased from FTpolymers. If not mentioned otherwise, all hydrogel solutions were prepared with 40 v/v% PEGDA and 60 v/v% deionized water (Millipore), 0.01 w/v% LAP (diluted in Millipore deionized water). For imaging, GFP or mCherry fluorescent particles (200 nm, 300 nm, or 5 µm)

were added at a concentration of 0.01 v/v% (or ≈ 7 x 10^9 nanoparticles of 300 nm per mL). All solutions were prepared at room temperature (RT) and magnetically stirred for 2 h. Sterilization of the hydrogel solutions was performed by filtering through a 200-nm filter before printing (Millex-GS Syringe Filter Unit, 0.22 µm).

2.2 Printhead fabrication process

The design and fabrication of the 3D printheads are illustrated in figure 2.A. The printhead body was fabricated with a commercial SLA 3D printer (DWS 29J+, DWS, Italy) offering a 40-µm XY resolution combined with a tunable 10- to 100-µm Z resolution, wavelength = 405 nm. We selected DL260 composite photosensitive resist (composite urethane-acrylate resist, Young's modulus ≈ 2 GPa, DWS Systems, Italy) as a base material. Batches of eight printheads were produced simultaneously using a printing speed of 5800 mm/s and slicing/hatching distances of 30 µm (corresponding to 1.1 kJ/cm^2; Fig. 2.A.I.). The printing proceeded for 3 h per batch. Once printed, the parts were developed by immersion in acetone at RT for at least 5 min in an ultrasonic bath (Elma S100H).

Protection and sealing of the optical fiber insert were performed using a 1 mm × 1 mm borosilicate glass slide obtained by dicing a 170-µm thick glass slide using a DAO321 system. Prior to glass slide integration, a small volume (50 nL) of glue (bicomponent epoxy adhesive Epotek 301, Ftpolymers) was delivered into the cavity surrounding the optical fiber aperture (Fig. 2.A.II.*).* The glass slide was further mounted on the printhead (Fig. 2.A.III.). Both glue and glass slides were bonded on the printhead with a microelectronic assembling machine (Tresky 3000). Bonding was performed at 70 °C for 1 h.

Finally, a PDMS layer was added to the top of the glass slide. This layer acts as a non-adhesive coating, as oxygen-based inhibition near the PDMS surface allows for hydrogel crosslinking while preventing attachment to the printing head during motion [24], [30]. We deposited an approximately 77-nL drop of PDMS (Sylgard 184; Fig. 2.A.IV) to obtain a dome with a 150-µm thickness. PDMS has good transparency at 405 nm, which prevents energy loss and provides an optical index that preserves the laser beam size. A ball-lensed optical fiber (BL-5 on high power single mode 405 nm fiber from WT&T) with focus distances between 200 and 3000 µm and a waist diameter of 7 µm was inserted in the printhead. The printheads are produced efficiently enough to be considered disposable if any alterity is

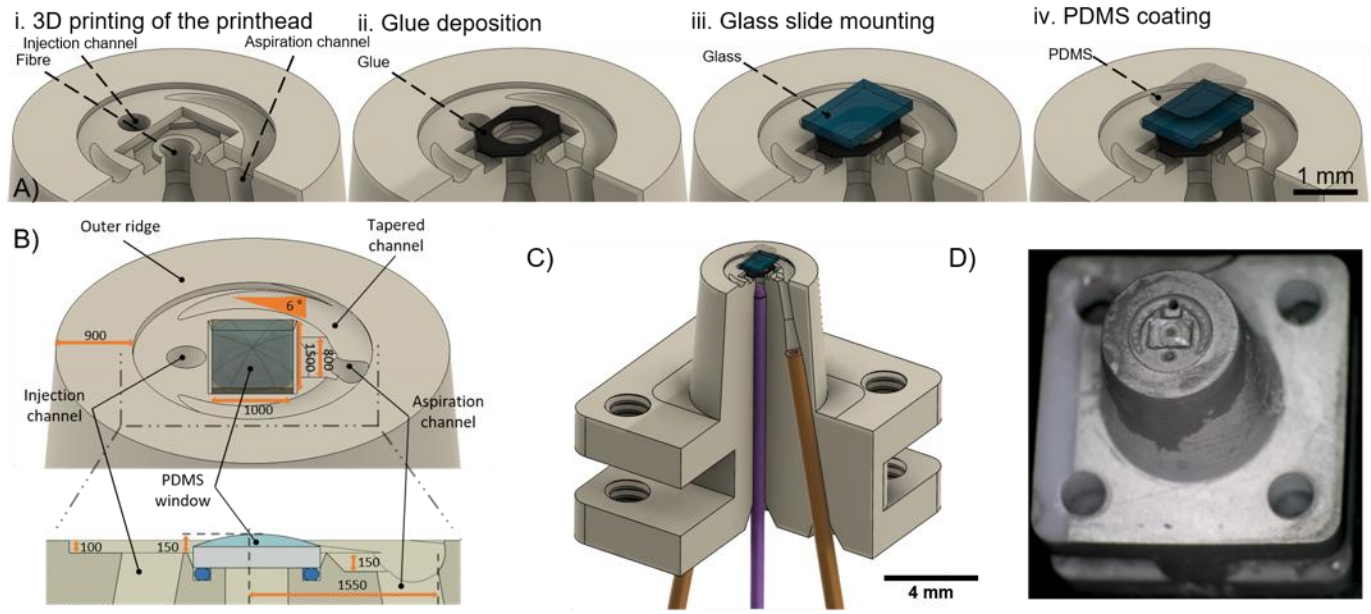

Figure 2. Printhead fabrication protocol. (A) Design of the printhead obtained by SLA 3D printing (i). A glass slide is bound to the printhead (ii–iii) and protected with a PDMS coating (iv). (B) Top view and cross cut image of the printhead structures and dimensions (values are given in µm). (C) Overall view of the printhead showing the structure of the injection and aspiration channels (orange) and the insertion of an optical fibre (purple). (D) Optical micrograph of an assembled printing head.

detected, after fabrication or a printing

2.3 Photo-polymerization control

The optical fiber was coupled to a 405-nm monomodal laser (Laserboxx from Oxxius) with adjustable power (P_{in}) ranging from 5 to 120 mW. To provide more accurate control of the beam intensity and compensate for the non-linear response of the laser intensity at low or high power, the laser driver was triggered with a function generator with 1 kHz square signals and a variable duty cycle to further modulate the intensity by a factor DC_{FG}. The effective output power was measured by positioning a Thorlabs S170C probe with PM200 power meter at 1 cm from the printhead apex.

To achieve different beam sizes, we modified the vertical position of the fiber in order to modulate the polymerization area by defocusing (Suppl. Fig. 1*)*. In high-resolution mode (HR, FWHM = 7–20 µm), the fiber was positioned to align the focus point at the printhead surface (PDMS dome) while in low-resolution mode (LR, FWHM = 50–100 µm), the fiber was positioned 400 µm above in order to enlarge the beam profile in the polymerization area. For a given laser intensity, displacing the fiber induces a variation of spatial distribution of light. Compensation of the dose was performed by dynamically adapting the laser input power (P_{in}) or the function generator duty cycle (DC_{FG}). For one isolated line, the surface dose was approximated as: $dose = P_{output}/(D_{spot} \cdot V)$ (1), where P_{output} (P_{output} =

$P_{input} \cdot k_{transmission} \cdot DC_{FG}$ (2)) is the laser power at the printhead apex, D_{spot} is the FWHM of the spot, P_{input} is the nominal input power, and $K_{transmission}$ is the light transmission factor between the laser emitter and printhead apex. By tuning both the FG duty cycle (0.1%–100%) and the input power (15–120 mW), we achieved an output power range from 0.7 µW to 21 mW, or 194 kW/m^2 to 584 MW/m^2 with R_{spot} = 6 µm.

Certain experiments (e.g., that illustrated in Section 3.3) were carried out using a dual fiber printhead (Suppl. Fig. 1.A). The printhead design was adapted to integrate two optical fibers. A computer-driven fiber switch (FFSW-122000323-MD, Laser Components) was integrated between the laser source and the fibers to switch between high-resolution and low-resolution modes.

2.4 Control of microfluidic injection

Buffer medium and photopolymerizable materials were introduced to 15-mL falcon tubes. Each tube was connected to a M-switch 10-to-1 microfluidic valve (Fluigent, France) allowing selection of the solution to be injected. The aspiration channel was connected to a 50-mL falcon tube. A Fluigent Flow-EZ air pressure controller was used to generate a positive pressure relative to P_{atm} in the injection tubes to drive fluids, while a Fluigent Push-Pull air pressure controller imposed a negative pressure (relative to P_{atm}) in order to promote fluid aspiration to the aspiration channel. The Flow EZ system was coupled to flowrate sensors (Fluigent Flow unit Medium ±80 µL/min or Large ±1 mL/min) allowing feedback control of flowrate in both the injection and aspiration channels. To favor HFC and prevent cross-contamination of the injected material in the medium surrounding the printing area, the flowrate ratio between aspiration and injection was adjusted according to the printing speed, material viscosity, and distance between the gap and surface (Z_{gap}), as discussed in part 2.2.

2.5 Printhead design

STL printhead designs were generated using Fusion360 (Autodesk, San Fransisco, USA). Hydrodynamic optimization and characterization of the printhead design was carried out through Comsol simulations (v5.5 Comsol Multiphysics, COMSOL AB, Sweden). The printhead consists of a conical device integrating one cylindrical port (diameter 550 µm) for optical fiber insertion as well as injection and aspiration channels for material delivery and recovery (Fig. 2.C). Guiding microfluidics structures were integrated at the apex of the printhead to control the spatial distribution of hydrodynamic resistance and material flow during injection (Fig. 2.B*)*. In particular, a circular tapered channel with increasing depth (R = 1.3 mm, r = 0.5 mm, maximum depth = 250 µm, angle = 6°) was integrated to guide the flow of injected material toward the printing area. An additional ditch (width = 600 µm, length = 800 µm, height = 150 µm) was placed near the aspiration channel in the axis of the polymerization point to guide the injected material toward the polymerization point. To further increase material recovery, a 900-µm wide and 100-µm high ridge was integrated at the periphery of the printhead to help isolate the injection and aspiration ports from the outer environment.

2.6 CFD Comsol simulations

CFD simulations were performed using the commercial finite element software Comsol Multiphysics. Numerical simulations involved both "*laminar flow"* and *"transport of diluted species*" modules through "*time dependent"* studies. The model 3D geometry was built in Comsol using the above specifications. The viscosity of the environmental solution (μ_{med}) was set to 1 mPa.s, as water, and if not specified otherwise, μ_{mat} was set to 8.5 mPa.s, which is the viscosity of a solution of 40% PEGDA 700 and 60% DI-water [31]. Printhead velocity is defined by slip boundary conditions on the printed structures (if present), exterior box, and support. The software calculates each point viscosity by linear evaluation depending on the point concentration of the injected and environmental material.

2.7 Instrumental platform and control software

The printing platform was integrated on a fluorescence microscope (IX71, Olympus) equipped with an XY-stage (MS-2000, ASI) with a range of 120 x 110 mm and a 1-µm repeatability. The printhead was mounted on a translation stage (LTA-HL, Newport) providing control of the Z position with 25-mm maximum displacement and a 3-µm repeatability. The Z stage was mounted on the microscope frame, thus allowing movement of the sample in the XY plane independently while maintaining the position of the printhead. The whole setup was integrated in a temperature-controlled enclosure (H201-T-unit-BL from Okolab).

All hardware components (XY-stage, Z-stage, pressure controllers, fluidic valve, laser, FG, fiber switch) were driven with a homemade LabVIEW (National Instruments) interface.. The software was designed to process Gcode (all required actions of the printer combined into a script) and transform coordinates in a list of trajectory vectors, including {moving speed, X movement, Y movement, Z height, laser state, material to be printed, flowrates, high/low resolution boolean, delay}.

2.8 Slicer development

The development of a multimaterial and multiresolution 3D printing process requires synchronizing the material injection, the adaptation of the laser beam, and the printing trajectories according to the features of the design. For those reasons, we developed a dedicated slicer software with Python. The vectorization was performed in five steps (Suppl. Fig. 2): i) slicing of the STL objects in the Z-axis; ii) selection of the material and optimum resolution for each slice; iii) filling of the design features according to hatching and velocity; iv) vector sorting depending on the printing strategy; and v) export of vectors dataset in specific Gcode format.

2.9 Substrate preparation

Printing was performed on 24 mm × 32mm × 170 µm glass slides (Menzel purchased from Fisher Scientific), treated with MAPTMS (Sigma Aldrich) for adhesion of the printed hydrogel. The glass slides were first washed with acetone, deionized water, and ethanol, then dried under a nitrogen stream. Then, the slides were activated using air-plasma treatment for 5 min (Diener PICO, 0.5 mBar, 40 kHz, 50 W). A solution of 1% MAPTMS and 0.3% acetic acid in DI water and 98.7% ethanol was prepared. The glass slides were immersed for 5 min, then rinsed with ethanol, dried with nitrogen, and stored under vacuum.

The glass slides were mounted on 75 mm × 50 mm microscope glass slides (Sigma Aldrich: 2947) using synthetic double-sided rubber, from which we can recover the glass slide after the printing (Tesa tape purchased from RadioSpare). On the perimeter of the larger glass slide, a rectangular PMMA frame with a thickness of 8 mm, fixed by double-sided tape, created a wall containing the buffer medium, for immersed printing.

2.10 Cell-culture and labelling

For the cell seeding experiments, substrates, tubes, and the environment were first sterilized with a 70% ethanol solution. PC3-GFP prostate cancer cells were seeded at a concentration of 10,000 cells/cm^2 and cultured for 3 days in 5 mL of medium (RPMI, 10% fetal bovine serum, 1 % penicillin-streptomycin-G418) at 37 °C under 5% CO_2. After 3 days, the cells were fixed with 4% formalin for 20 min and permeabilized in 0,2% tritonX-100. The cell nuclei were stained with DAPI solution at 0.02 mg/mL for 5 min. After staining, the samples were stored in PBS solution at 4 °C.

For the spheroids experiments, human adipose derived stem cells (hASCs) were isolated from abdominal dermolipectomy waste (Plastic Surgery Department, CHU Toulouse, France) from female donors, as previously described [32]. The experimental protocols were approved by the French Research Ministry's institutional ethics committee (No: DC-2015-23-49) and informed consent was obtained from all subjects in accordance with institutional guidelines on human tissue handling and use. hASCs were plated and amplified in endothelial cell growth medium-2 (EGM2, Promocell) containing 0.1% (v/v) amphotericin B (Life-Technologies) and 1% (v/v) streptomycin/penicillin (Life-Technologies). The medium was changed every 2-3 days. When the cells reached 80% confluency, they were harvested and hASC spheroids were generated by seeding 50,000 cells in 50 µL of EGM2 medium in ultra-low attachment (ULA) 96-well round-bottom plates (Corning Incorporated Life Sciences) and maintained overnight under stirring (150 rpm). Cells were kept in EGM2 (150 µL added at day 1) medium until spheroid formation, i.e., 1–2 days after seeding. Spheroids of hASCs were individually handled and deposited in each cavity of the PEGDA structure on fibronectin-coated glass coverslips (solution at 10 µg/mL fibronectin, 37 °C overnight and washed with PBS) in a minimal volume of EGM2 medium to cover the entire structure. The spheroids were allowed to settle for several hours at 37 °C to promote attachment of the spheroids to the glass surface before further addition of EGM2 medium. The spheroids were maintained for 3–6 days and the EGM2 medium was changed every 2–3 days. After culture, PEGDA structures containing spheroids were washed in PBS and fixed with 4% paraformaldehyde overnight at RT. Samples were then permeabilized and blocked in PBS solution containing 1% Triton X-100 (Sigma) and 3% horse serum (Jackson Immunoresearch) for 3h at RT. Next, samples were incubated with Alexa Fluor™ 488 Phaloïdin (1/500) in PBS containing 1% Triton X-100 and 1% horse serum for 3 h at RT. After PBS washing, nuclei were stained with 2 µg/mL DAPI for 1 h at RT (Sigma, USA).

2.11 Imaging

Scanning electron microscopy (SEM) imaging was performed with a Hitachi S-3700N for printheads and hydrogel structures (dried under standard atmosphere for vacuum imaging). Images 3.A, 6.C-F, 7.B, 8.A-C, 8.G, 9.A/E, graphical abstract, Suppl. images 1. and 6.G., and Suppl. Video 1 were taken with an inverted microscope IX71 Olympus, DAPI, FITC or mCherry filters and a Nikon DS-Qi1Mc camera. Images 6.A-B, 7.A, 9.B-D/F were taken with a confocal Leica SP8. Image 2.D. was taken with a Dino camera. Images were analyzed with imageJ [33] using the 3D TransformJ plugin [34].

3 Results & Discussion

3.1 Description of the opto-microfluidic printing concept

Similarly to microfluidic probes [27]–[29], the 3D-Flowprint printhead consists in a microfluidic device with one injection and one aspiration channel for local delivery of a stream onto a surface (Fig. 1). This microfluidic delivery has many advantages, i.e., low volume consumption, multiplexing, local material delivery, and control of material composition. Optimized open microfluidic channels on the surface of the printhead (see part 2.5) and precise control of the injection and aspiration flowrates (see part 3.2) enable hydrodynamic flow confinement (HFC) of the injected material and prevent cross-contamination in the medium.

To create these open microfluidic channels, the use of 3D printing technologies, in particular SLA, provides unique advantages for the prototyping and optimization of the microstructured volume and surface of the printhead (see part 2.2). Moreover, it offers a reliable low-cost and simple approach to the construction of 3D microfluidic devices with resolutions at the micrometric scale [29], [35], [36] that are largely impossible with standard photolithography or molding approaches.

The hydrogel solutions to be injected inside the printhead are photopolymerizable liquid materials with viscosities relatively close to that of water (μ_{mat} = 8.5 mPa.s for our main solution) [37]. Unlike micro-extrusion or droplet-based techniques, this printer does not require specific material characteristics such as shear-thinning properties or surface tensions adapted for droplet formation [37], [38]. We focused our interest on poly(ethylene

glycol) diacrylate (PEGDA), which is recognized for the development of hydrogel scaffolds and 3D models of microenvironments [39].

Between the injection and aspiration channels, a closed third channel contains a ball-lensed optical fiber (Fig. 1.B) with a focus waist diameter between 7 and 100 µm. It provides a near-collimated light all the way from the printhead to the previous slice. The illumination activates the photo-initiator lithium phenyl-2,4,6-trimethylbenzoylphosphinate (LAP), which is cleavable at 405 nm, resulting in two radically activated species. The formers initiate a chain reaction on the double carbon bonds of the hydrogel methacrylate groups to create a network, turning the liquid injected solution to a solid at the polymerization spot [40], [41]. In this work, we used mainly PEGDA hydrogel and LAP photo-initiator (40% PEGDA 700, 60% PBS, 0.01% LAP), which are both biocompatible at the stated concentrations [39], [41], [42]. Then, as with most 3D-printing technologies, an XYZ computed itinerary constructs the 3D object vector-by-vector (Suppl. Fig. 3 and Suppl. Video 1). To increase printing speed and to add more versatility to the printer, we also implemented multi-resolutions printing.

3.2 Microfluidic characterization

3.2.1 Hydrodynamic flow confinement

Multimaterial printing systems impose a fast and efficient renewal and removal of material in the printing area to prevent contamination of the surrounding medium with unpolymerized material. Here, the small gap between the printhead and the printing substrate induces high hydrodynamic resistance between the injection and aspiration ports that limits the flow of material in the printing area and favors its spreading outside the printhead. A careful optimization of the printhead design to limit such spreading and control the distribution of flows was performed using hydrodynamic simulations and subsequently validated experimentally.

As shown in figure 3, the printhead geometry was designed to ensure a continuous flow of material in the exposure area and the confinement of the injected material in the printing area. The injection channel was placed at the nearest point to the PDMS dome to (i) decrease the distance between the injection channel and the polymerization point; (ii) decrease the distance between the injection and aspiration channels; and (iii) increase the distance between the injection channel and the surrounding medium. In order to further enhance the hydrodynamic confinement, the printhead integrates a buried structure at its periphery that is composed of a circular tapered channel that connects the injection port to the aspiration port, with increasing depth toward the latter (Fig. 2.B). The hydrodynamic resistance and pressure drop induced along this structure favors the orientation of the flow towards the aspiration channel and through the exposure area. In order to further enhance this confinement effect, a 900-µm-wide and 100-µm-high ridge at the periphery of the printhead helps isolate the injection and aspiration ports from the outer environment.

Figures 3.A and 3.B provide a comparative study between experimental characterization and computer fluid dynamics (CFD) simulation of the hydrodynamic flow distribution in the printing area. In this experiment, the distance

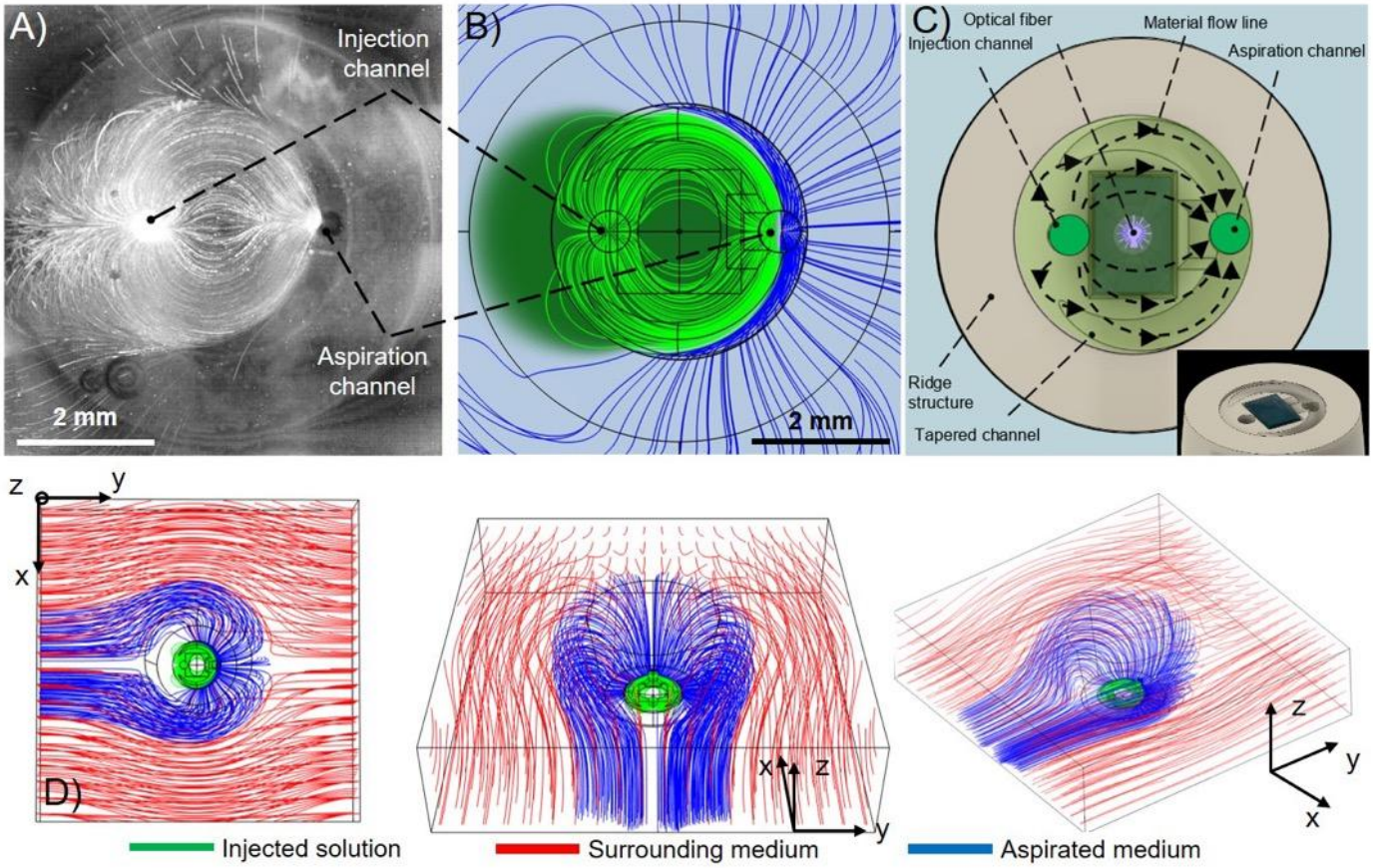

Figure 3. Characterization of flow distribution around the printhead. (A) Experimental analysis showing the simultaneous injection and aspiration of a suspension of fluorescent particles. (B) Comsol simulations performed according to experimental parameters. (C) Schematic of the structure and topography of the printhead: A tapered microchannel associated to a circular ridge structure are used to induce hydrodynamic confinement of the injected material. (D) Three views showing the 3D distribution of flow obtained from Comsol simulations. (A-B-D) Parameters: V = + 0.1 mm/s, Z_{gap} = 100 µm, μ_{mat} = 8.5 mPa.s, μ_{med} = 1 mPa.s, φ_{in} = 25 µL/min, Rφ = 5. (B-D) Green, blue and red flow lines represent the flow distribution of respectively the injected material, the aspirated medium and the surrounding medium.

Z_{gap} between the printhead and surface was set to 100 µm. A suspension of 5 µm fluorescent particles (at 0.01% v/v) was added to our standard PEGDA 700 solution, which was used to monitor the flow distribution of the injected material. In this first series of experiments, the printhead was kept immobile to better analyze the effect of the printhead topology on the flow distribution. The injection flowrate was set to 25 µL/min while the aspiration channel flowrate was set to 125 µL/min. The pictures in figure 3.A-B are the flow trajectories along the plane XY, seen from below the printheads. For figure 3.A, a video was taken, and frame intensity maximums, indicating the position of nanoparticles in each frame, have been extracted and summed to obtain the nanoparticles paths. As can be seen in figure 3.A, a cardioid-like flow distribution pattern is observed. Figure 3.B. shows the distribution of hydrodynamic flow lines during material injection (in green for the injected material and in blue for the surrounding medium). There is a qualitative agreement in flow-line distribution between the experimental results and numerical studies. All visible flow lines associated with the material injection are directed towards the aspiration port. Moreover, a significant fraction of the flow lines directed towards the aspiration port is associated with the surrounding medium. These flow lines surround the limits of the injection area and confirm the confinement of the material within the printhead footprint.

On the left of figure 3.A, some nanoparticles can be seen, at low speed, on the external edge of the confined area. By varying the hydrodynamics parameters, this phenomenon might lead to notable material loss and potential cross-contamination. The parameters influencing this phenomenon are investigated in the next section.

3.2.2 Influence of Z_{gap}, flowrate ratio, and V on flow confinement

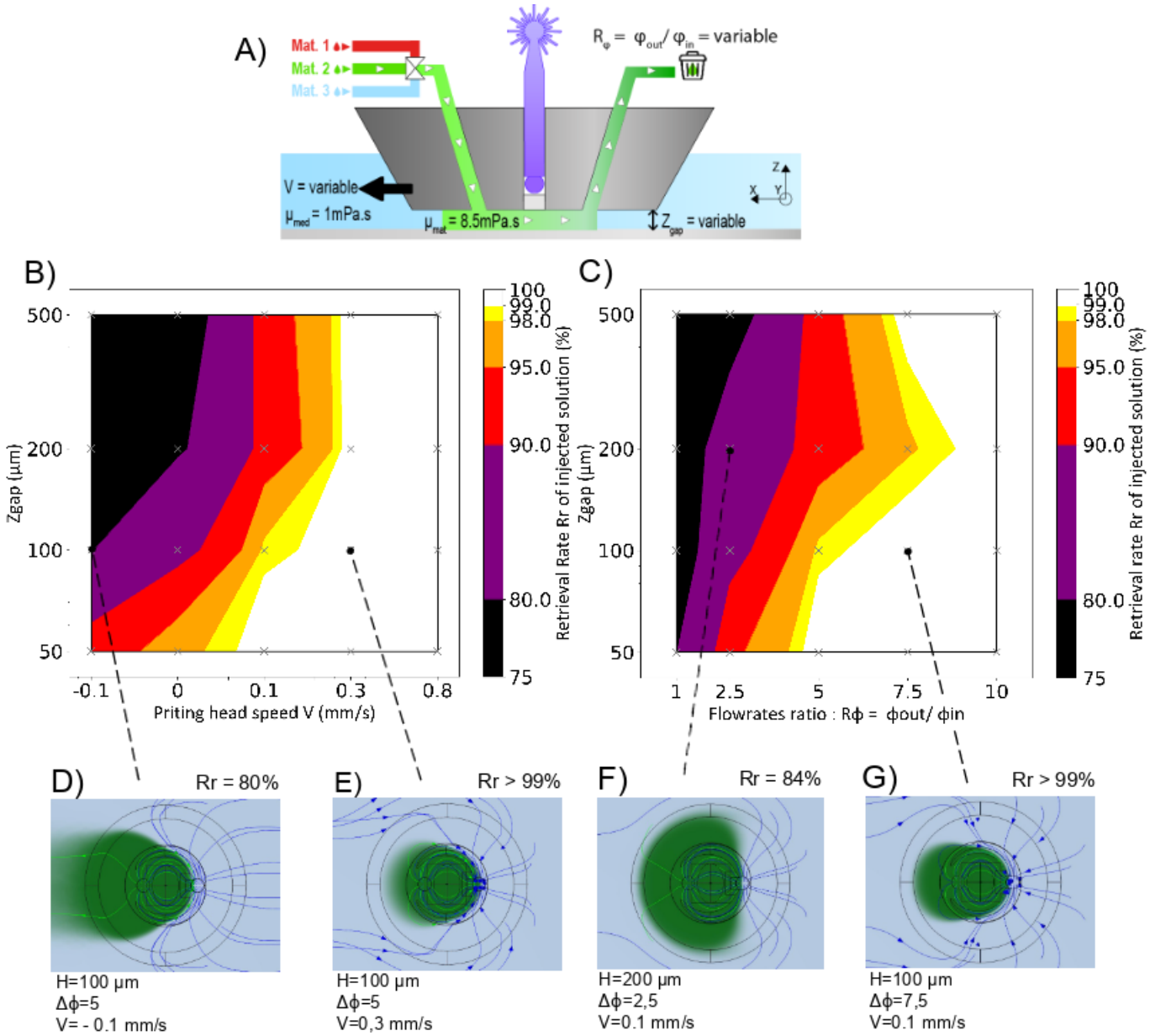

Figure 4. Numerical simulations (Comsol) showing the influence of flowrate ratio Rφ, printhead velocity V and Z_{gap} on hydrodynamic flow confinement (HFC) (μ_{mat} = 1 mPa.s and μ_{med} = 8.5 mPa.s). (A) Schematic illustration of the main parameters investigated in this study. (B) Diagram showing the impact of V and Z_{gap} on the HFC. Rφ = 5. (C) Diagram showing the impact of Rφ and Z_{gap} on the HFC. V = 0.1 mm/s. (B–C) Grey crosses show data points obtained through Comsol simulations. Color codes were generated by interpolation between data points. (D-E-F-G) Images are Comsol top-view cross-sections (at mid-Z_{gap}) for injection of green material in blue medium with the conditions listed below. Images (E) and (G) illustrate typical low-confinement situations giving rise to material loss in the surrounding medium.

Estimation of the retrieval rate Rr (Rr = collection of the polymerizable material over injection) was measured through numerical simulations to study this phenomenon quantitatively. An exhaustive analysis of the evolution of the Rr depending on printhead velocity V, Z_{gap} and flowrate ratio ($R\varphi = \varphi_{out}/\varphi_{in}$) was performed through Comsol simulations (Fig. 4). At time t = 0 s, the entire system is filled with the first solution (in blue), representing the medium with μ_{med} = 1 mPa.s. Then, during the study, a continuous inflow of a second material with μ_{mat} = 8.5 mPa.s (in green) was applied on the injection channel at φ_{in} = 25 µL/min. A similar flowrate-controlled outflow was applied to the aspiration channel at the value $\varphi_{out} = -R\varphi*\varphi_{in}$ (typical flowrate ratio was Rφ = 5). The simulations ran until t = 50 s (which is beyond equilibrium when HFC is maintained). The in-plane printhead velocity V is represented by adding a flow-condition on the support and the exterior box, with typical value V = +0.1 mm/s. The images are top-view, and the black lines represent the outline of the printhead geometry.

As seen in figure 4.B–C, for Z_{gap} < 200 µm, the flow confinement is improved (higher Rr) when drawing closer to the surface due to the increasing influence of the printhead surface structure. The hydrodynamic confinement induced by the printhead architecture increases significantly as the distance between the printhead and the surface decreases to the order of magnitude of the ridge and the other surface structures. Lower Z_{gap} is favorable to the printing of thin structures, yet HFC is still attainable at higher Z_{gap} up to 500 µm (with an appropriate flowrate ratio, as seen in Fig. 4.C), presenting the possibility of printing of high structures. Increasing the printhead velocity along the positive X-axis favors material recovery as this contributes to the motion of material towards the aspiration channel. For example, with Z_{gap} = 100 µm and Rφ = 5, Rr is 88%, 98%, and 100% (Fig. 4.E), respectively, at V = 0 mm/s, 0.1 mm/s, and 0.3 mm/s. Conversely, moving the printhead backward contributes to the spreading of the material outside the printhead area, thus reducing HFC. As an example, Rφ = 5 is not sufficient to maintain HFC with backward motion V = -0.1mm/s for all Z_{gap} (Fig. 4.D).

Figure 4.C confirms the expected influence of Rφ on the HFC, demonstrating that higher Rφ leads to better confinement for every Z_{gap}. We observed that Rr > 99% can be obtained at low Rφ (Rφ = 5) with Z_{gap} = 50 µm while Rφ has to be increased (Rφ ≥7.5) to reach the same level of recovery when increasing Z_{gap} above 100 µm (Fig. 4.G) to avoid cross-contamination, as seen in figure 4.F.

3.2.3 Influence of material viscosity

When compared with the surrounding medium (typically a water-based medium with viscosity (μ_{med}) = 1 mPa.s), injected materials with different viscosities (μ_{mat}) may modify the flow distribution and therefore Rr. Numerical simulations were performed with different values of μ_{mat} ranging from 1 to 10 mPa.s while keeping μ_{med} at 1 mPa.s (V = 0.1 mm/s, Z_{gap} = 50 µm, Rφ= 2.5). The HFC decreases because a more viscous material tends to be less aspirated, leading to the environmental solution taking over in the aspiration channel. By increasing the viscosity by a factor of 10, Rr only decreases from 100% to 92% (Suppl. Fig. 4), meaning that the viscosity of the injected material has a low impact on the flow distribution.

3.2.4 Multimaterial injection and flushing

Sequentially flushing and injecting different materials is essential for multimaterial printing, with fast and complete removal of the previous material required to avoid cross-contamination. The printhead was designed as an integrated microfluidic device connected to a library of materials through a manifold and rotating valve (see part 2.4), allowing switching during printing from one material to another. We investigated this protocol first by the replacement of PEGDA 700 (µ=8.5 mPa.s) loaded with green fluorescent 300-nm particles with PEGDA 700 loaded with red fluorescent particles using typical flowrates (φ_{in} = 30 µL/min, Rφ = 5, V = 0, and Z_{gap} = 100 µm). After 60 s, more than 90% of the first material was removed and replaced (Suppl. Fig. 5.A). This measure integrates the time required for the solution to fill the dead volumes between the valve and the printhead and considers Taylor diffusion. Then, the flushing of the PEGDA 700 material by a less viscous buffer medium (µ = 1 mPa.s) was performed at the same typical flow rate and at higher flowrates (φ_{in} = 60 µL/min, Rφ = 5). The results suggest a quasi-linear influence of the flushing time with flowrate, with a replacement ratio of 90% at 15 s and 30 s, respectively, for high and typical flowrates (Suppl. Fig. 5.B).

3.3 Material photopolymerization during injection

3.3.1 General concept of the opto-fluidic polymerization

Our initial experimental and numerical studies demonstrated the possibility of dynamic control of the confinement and sequential injection of photopolymerizable materials in the exposure area. Our next studies were devoted to demonstrating the photopolymerization of the materials during injection and to the characterization of the printing process. Contrary to conventional SLA or 2PP methods, in which the photosensitive material is processed under static conditions, the material here is in movement during the photopolymerization process, reminiscent of continuous flow lithography [25], [43] where a flow of material is polymerized while flowing in a confined microfluidic channel. With such a process, as demonstrated in these studies, a careful investigation of the coupling between of the laser power and printhead velocity is required to determine the impact of the hydrodynamic flow on the polymerization process and resolution.

Our first validations were performed by the printing of line arrays (such as in Fig. 5.A) using PEGDA solutions. Figure 5 shows typical examples of PEGDA features printed for a Z_{gap} value of 50 µm and observed through confocal and bright field imaging. Figure 5.C shows lines of 10 µm with decreasing distances between them until reaching the width of a single line. Most printings were realized in the positive X-axis direction, yet it is possible to print in any direction, as shown in figure 5.B/D.

These results confirmed that the effect of laser pulse time (blinking with a square signal at DC_{FG} = 1 kHz, see part 2.3) on the polymerization process is not noticeable. The distance traveled by the printhead between two pulses (d_{pulse} = V/DC_{FG}) in the common velocity range 0.05–0.8 mm/s varies between 0.05 and 0.8 µm, which can be considered negligible compared to the laser spot size.

We also investigated experimentally the spatial distribution of light intensity provided by the optical fibers coupled to the 405 nm laser source (see part 2.3). Sliding the fibers in the printhead indeed induces a defocusing effect that modifies the intensity distribution and controls the spot size (Suppl. fig. 1). For example, suppl. figure 1.B. shows the spatial distribution of light intensity in the exposure area for two optical configurations that were obtained by adjusting the vertical position of the fibers in the printhead (0 and 600 µm). In this configuration, the laser spots were

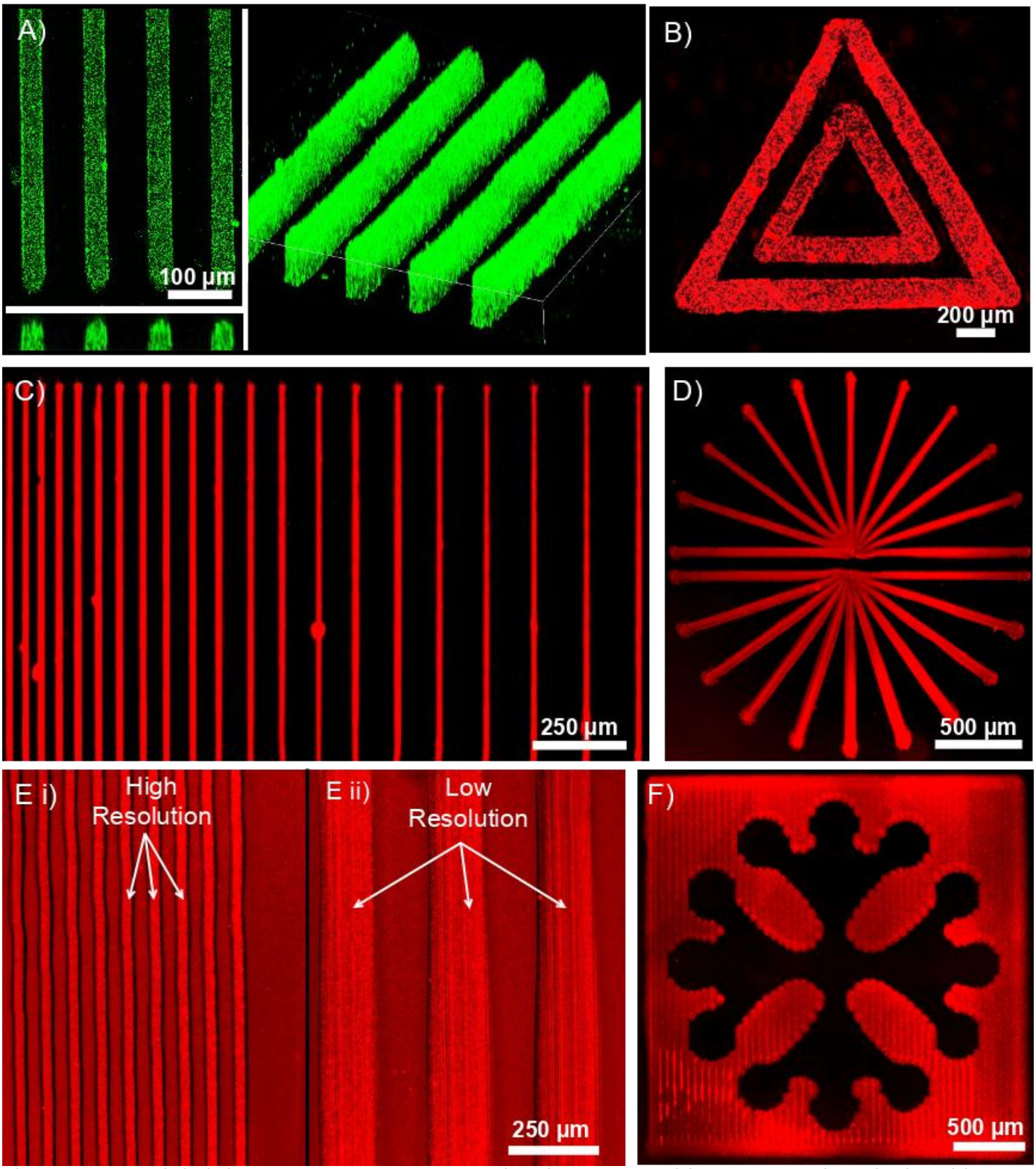

Figure 5. Images of single-layer PEGDA structures. Suspension of 200 nm GFP (A) or 300-nm mCherry (B-F) particles were added to the material for better visualization. (A) Array of lines with constant spacing (top view, cross-section, and 3D view). (B) Intricated triangular structures. (C) Array of lines with varying spacing (30–150 µm). (D) and varying printing orientation). (E) Multiresolution printing of lines with two optical fibre configurations leading to different line widths of 35 and 160 µm. (F) Printing of a large-scale cross structure. (A-B) Confocal images. (C-D-E-F) Fluorescence images.

estimated to be around 6 and 17 µm (FWHM measured with Z_{gap} = 50 µm). The profile of the energy distribution shows a good homogeneity over large Z distances (>200 µm) allowing the processing of thick material layers. The optical fibers and printheads are easily changed, allowing different spot sizes and widths of printed lines across experiments. A small spot size (6–40 µm) was mainly used to benefit high-resolution printing (i.e., Fig. 5.C/E.i, Fig. 6), while a larger spot size (up to 200 µm, i.e., Fig. 5.A/B/E.ii, Fig 7.A) was favorable for stability and quicker printing.

3.3.2 Influence of printhead velocity and output power during photopolymerization

In-flow photopolymerization was investigated through systematic modulation of the output power P_{out} and printhead velocity V by measuring the printing resolution. To be consistent with the hydrodynamic studies performed earlier, we investigated V in the range 0.05–0.8 mm/s, which is known to be compatible with hydrodynamic confinement conditions (Rφ = 7.5, φin = 25 µL/min), and we varied P_{out} in the range 0.0525–0.4 mW. For each P_{out} and V combination, the minimum dose required to create stable structures was estimated and the structure dimensions were measured (Fig. 6.A). The minimum line width obtained experimentally was 20 µm for several combinations of P_{out} and V corresponding to a threshold dose of 3750 mJ/cm^2 (see part 2.3 and eq. 1) and can be associated with a ratio P/V = 0.74 mJ/mm. As expected, the line width value increases with dose up to a value close to 160 µm. The results reveal a logarithmic dependence of line width on P_{out}/V (Suppl. Fig. 6). We could fit the curves to eq. 3:

$$Width(P_{out}, V) = k_1 \cdot \ln(k_2 \cdot P_{out}/V) \quad (3)$$

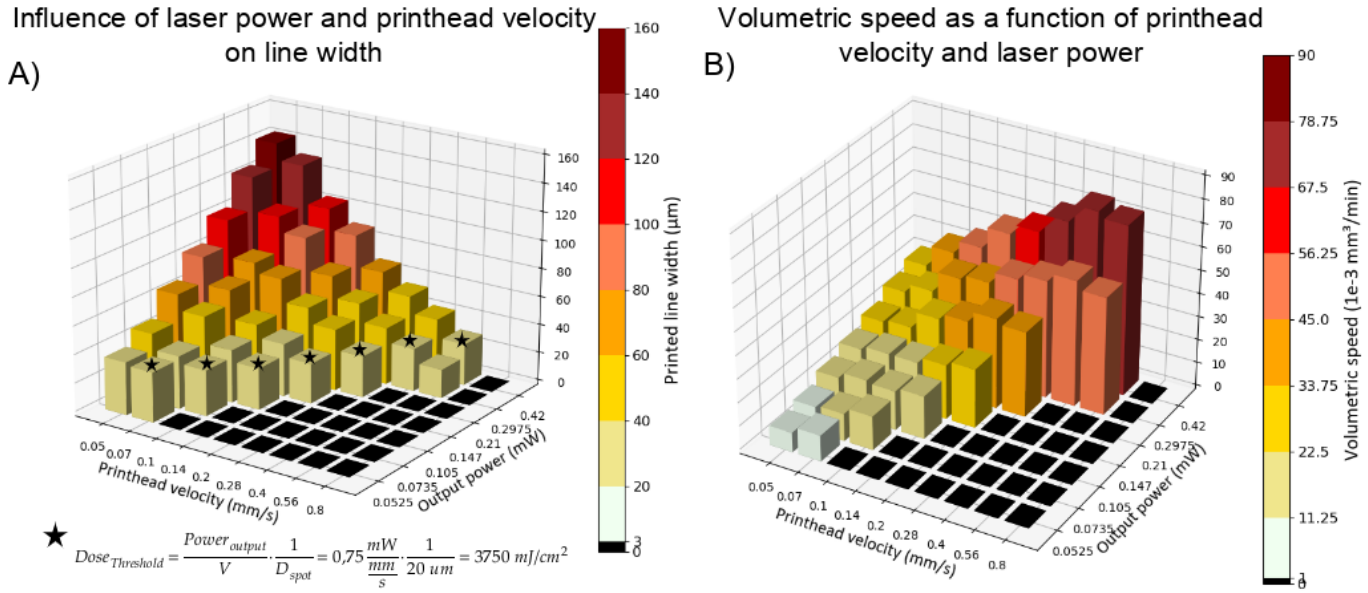

*Figure 6. Study of the in-flow photopolymerization. (A) Influence of the optical output power and printing speed on line width. Experiment realized with h = 75, φ_{in} = 25 µL/min, and Rφ = 5. Dose threshold values correspond to the minimum dose giving rise to stable structures (marked with a *). (B) Volumetric printing speeds based on the data in Fig 6.A data and eq. 4.*

with k_1=44.82, k_2 = 2.376, and R^2 = 0.9704.

3.3.3 Influence of pre-existing structures on the printing process

The exposure dose is associated with the residence time of the material in the area covered by the laser spot. This residence time correlates with the velocity of the material relative to the optical fiber, resulting both from the velocity of the printhead relative to the substrate and from the velocity of the material relative to the printhead. A question naturally arising when considering material inflow is the impact of preexisting structure at the proximity of the exposure area. Indeed, the printing process occurs in a continuous manner with the motion of the laser spot according to the programmed trajectory. Structures may modify the distribution of velocities, affecting the photopolymerization dose and impeding material supply during printing.

Simulations performed at φin = 25 µL/min, Rφ = 5 showed that on flat substrates with no pre-existing printed structures, the velocity of the solution relative to the head is around 0.5 mm/s in the polymerization area (measured at mid-Z_{gap} = 25 µm, Suppl. Fig. 7.A). When considering the presence of structures, simulations confirmed a significant reduction of the material velocity. In the vicinity of a pre-existing printed line, solution velocity drops to 0.1 mm/s (printhead velocity), as can be observed in supplementary figure 7.B. During the printing of a continuous layer (Suppl. Fig. 7.C.), the fluid is also slowed by the previously printed adjacent lines on the side. In both cases, the reduction of material velocity near the printed structures reduces the impact of material inflow and aspiration on the photopolymerization process that propagates progressively in the vicinity of the structure being processed.

The nearly constant width of printed lines in figure 6.A when keeping a constant P/V factor confirms that the dose is linked to the velocity of the printhead motion and that the motion due to the injection and aspiration flow is negligible. This observation provides an additional illustration of the decoupling between the photopolymerization and the hydrodynamic aspects (related to mass transport through injection and aspiration). For the start of new lines, no structures are already present, so the speed reduction is not effective. To overcome this limitation, we implemented over-dosing for these circumstances, which was achieved by a pause of 0.2 s before starting the printhead motion.

3.3.4 Printing resolution and correlated printing time

Figure 6.A shows a minimum linewidth of 20 µm for a laser spot size of 16 µm. The linewidth is almost always bigger than the laser spot size, due to chemical diffusion of reactive species, light dispersion and over-dosing above the polymerization threshold.

Figure 6.B shows the evolution of the volumetric printing speed according to the printhead velocity and output power in the same range of values as shown in figure 6.A for Z_{gap} = 75 µm. The volumetric printing speed is given by $V_{printing}^{xyz} = V \cdot width \cdot height$ (4). We observed a logarithmic influence of the printhead velocity on the width (see eq. 3), meaning that the best strategy for increasing the overall volumetric speed and decrease the printing time is to increase the printhead velocity. The variation of the width by modulation of P_{out} and V is advantageous as it allows tuning the width of printed features. From this perspective, increasing the laser spot size by switching to a larger spot size configuration should be preferable as compared to increasing the output power. Figure 5.E. demonstrates this capacity by the printing of two line arrays using a dual fiber head (high-resolution fiber on the left and lower-resolution fiber on the right). This feature could also be used to adjust the overlap between adjacent lines when considering the printing of merged lines to create a bulk object [44]. Using two fibers inside the printhead could also allow multi-wavelength printing for more specific multimaterial printing, such as that proposed by Ravanbakhsh in 2021 [6].

3.4 Processing multilayered and multimaterial 3D structures

3.4.1 Control of layer thickness

The creation of 3D structures through additive manufacturing processes requires accurate and reproducible control of the thickness of each printed layer. With 3D-FlowPrint technology, the layer thickness is defined by the geometrical confinement between the PDMS window and the support, i.e., the Z_{gap} value. Consequently, the Z_{gap} value is directly associated with the layer thickness as provided by the slicing software (see part 2.8). Figure 7.B shows an example of structures obtained for V = 0.1 mm/s at three different programmed heights (60, 80, and 120 µm). Each line was printed in a single passage, programming Z_{gap} to the desired thickness value. Interestingly, the three structures show almost constant lateral dimensions (~30 µm), demonstrating the low influence of Z_{gap} on lateral feature dimensions, and thus a limited spreading of light distribution in the layer.

We performed a more systematic study of the correlation between the vertical position of the printhead and the resulting structure thickness for values up to 350 µm. We implemented a fiber with large spot size (100 µm) resulting in an enlargement of the lines up to 150 µm. The dose was maintained constant during the experiment. Figure 7.A shows a ladder structure with programmed heights varying from 100 to 350 µm in 50-µm increments. Each segment of the structure was printed in a single passage by adjusting Z_{gap} to the target thickness. Confocal

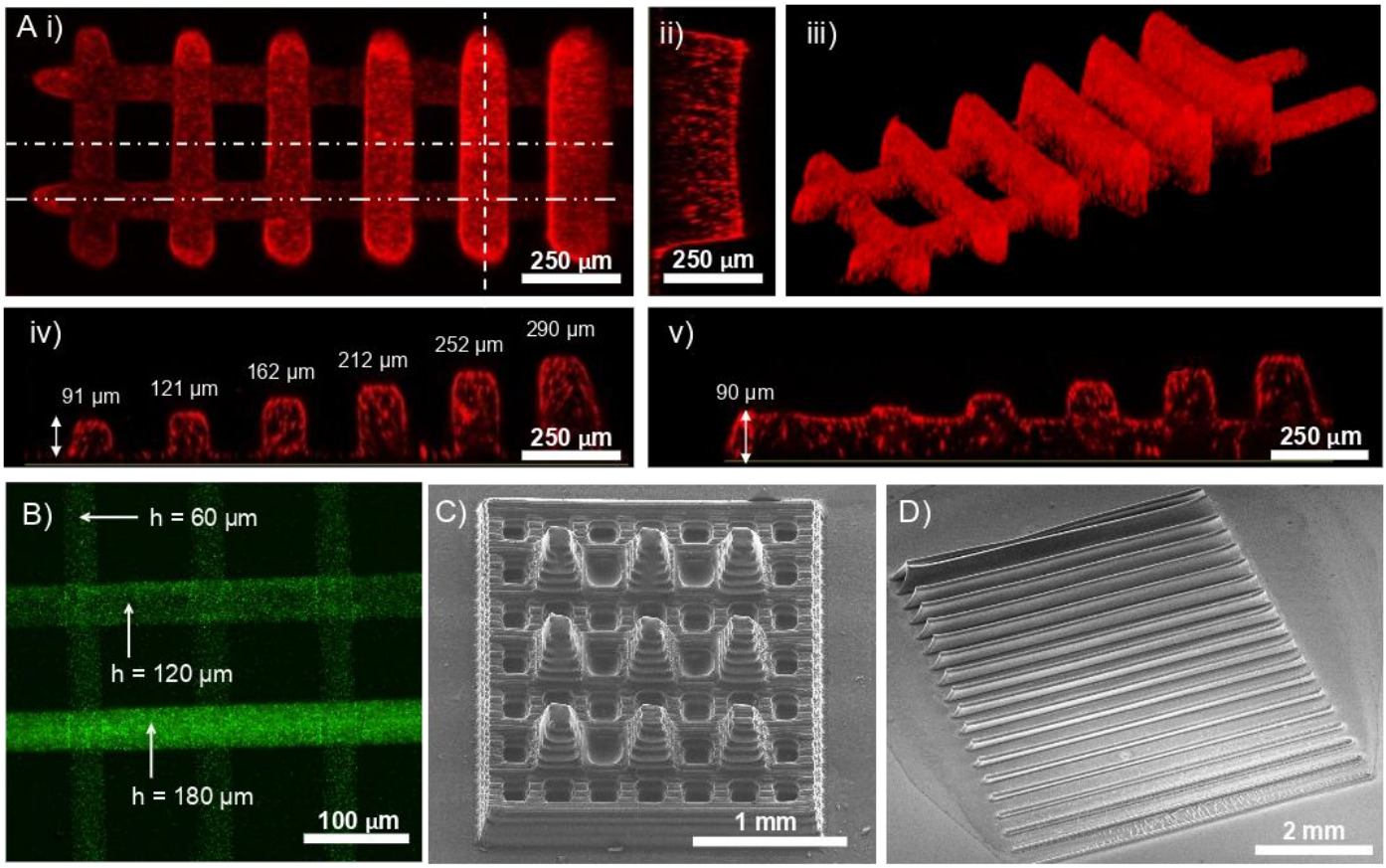

Figure 7. 2.5D and 3D PEGDA printed structures. (A) Confocal pictures of a ladder structure with segments printed at varying heights (h = 100 or 350 µm). (B) Fluorescence image of crossing lines successively printed with three different printing heights. (C) SEM image of a millimetric 3D structure, including protruding and recessed pyramidal features. (D) SEM image of an array of lines with varying heights (h = 20–400 µm).

observations revealed a 16% shrinking of the structure in the Z-axis. In the cross-section shown in figure 7.A.iv., orthogonally to the lines, we can see the accurate shape, while slight slopes (5°) are visible at the beginning and the end of lines in figure 7.A.ii due to shrinkage.

This experiment demonstrates the ability to produce, independently from the printhead velocity and output power, structures with a wide range of thicknesses. This observation first confirms the low light absorption in the polymerization layer, which is negligible in the range of dimensions investigated. This is made possible by the transparency of the injected PEGDA-based material. The hydrogel solutions indeed exhibit a low absorbance coefficient (≤0.01 m^{-1}) [45] that allows vertically uniform polymerization of the hydrogel layer. Thus, the polymerization of such PEGDA formulations does not show mechanisms related to front polymerization that may have arisen in absorbing samples [46]. Optimizing the transparency of the material is thus a clear advantage in terms of writing speed when considering the processing of thick material layers. However, this feature underlines one of the limits of the printing system when considering the creation of hollow structures or overhangs that might require careful adjustment of light absorption to benefit from the front polymerization mechanism.

3.4.2 Raster-printing protocol with positive and negative X velocities

The printhead was designed to ensure efficient confinement and recovery of the material by creating a preferential pathway, with low hydrodynamic resistance, towards the aspiration channel. This resulted in an asymmetric design that favors the flow of the material along the X direction from the injection port to the aspiration port. However, because of the no-slip boundary conditions, the printhead motion relative to the substrate modifies hydrodynamic flow in the exposure area. As illustrated in figure 4.D, moving the printhead in the negative direction may impede hydrodynamic confinement and favor loss of material in the surrounding medium. Even if we could still demonstrate the ability to print in 360° as shown in figure 5.D, polymerization was thus preferably performed following the positive X-axis direction. The printing of extended structures was processed using a conventional raster method (Suppl. Fig. 8.B). In each layer, the slicing software decomposes the features in an array of adjacent vectors oriented along the X direction. The trajectory of the printhead follows the first vector with laser on (green). Then, the laser is turned off along the second vector (dashed red) and the printhead is positioned at the beginning of the third vector. According to the expected line width, a 10% overlap between each laser passage was implemented to ensure cohesion of the final structure. In order to further limit potential loss of material during the repositioning of the

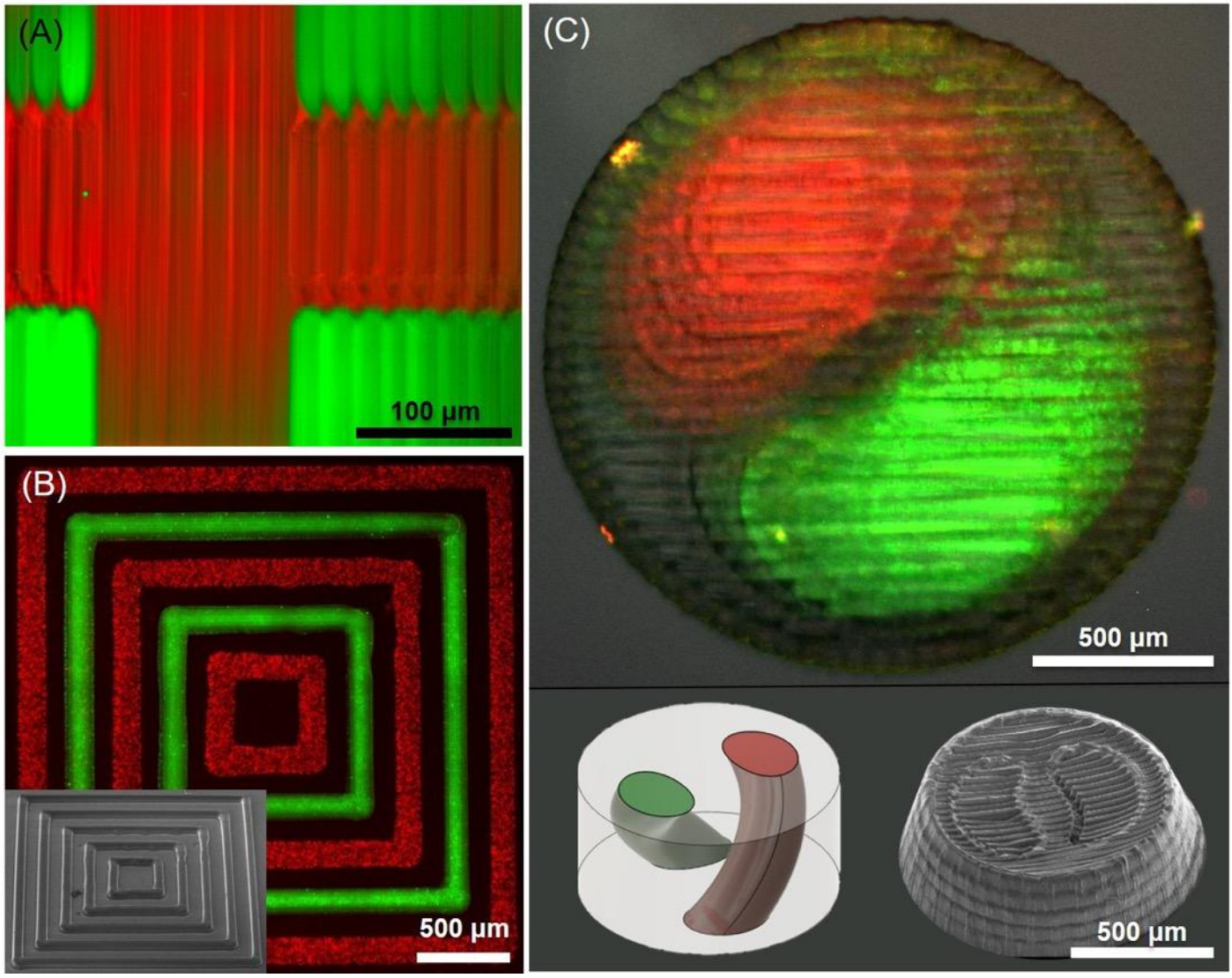

Figure 8: Figure 8. Demonstration of multimaterial printing. (A) Successive printing of segments showing low cross contamination and alignment resolution, h = 50 µm.(B) Concentric squares printed from larger to smaller, h = 50 µm.(C) Double helicoidal structure, h = 500 µm. Lower left and right corners show a CAD image and a SEM image of the printed structure. (A-B-C) All made from PEGDA solutions (with 300-nm mCherry particles for red, 200-nm GFP particles for green, and no nanoparticles for grey).

printhead, the Rφ ratio was dynamically adjusted during the process, i.e., Rφ = 5 during printing and increased up to Rφ = 10 during repositioning (with V = 0.1 mm/s and Z_{gap} = 50 µm; see Suppl. Fig. 8.B). We could prove the efficiency of our printing method by creating a French Occitan cross, as shown in figure 5.F.

We demonstrated the robustness of this printing process for the creation of millimetric-scale multilayered structures, such as that presented in figure 7.C. This structure integrates an array of pyramidal features with a 500 µm x 500 µm base and 500 µm height. In this experiment, the printhead velocity was set to 0.5 mm/s while the Z_{gap} value was set to 75 µm and maintained constant for each of the eight layers composing the final structure. The printing was performed in 6 h (Fig. 7.C.). Interestingly, this capacity of printing for long periods demonstrates the stability of the printing process. On the one hand, it shows that all along the printing, the injection/aspiration strategy allows for a continuous supply of photopolymerizable material to the exposure zone, even in the case of high-aspect-ratio structures such as those presented above. On the other hand, the spot size and associated printed voxel width remained identic along the experiment and the printing head PDMS showed no sign of bleaching. It points out the durability of the printheads.

3.4.3 Material switching

An example of material switching while printing is presented in Suppl. Video 1 (at video speed x8). Figure 8.A-B-C shows several proofs of concept for multimaterial printing using different solutions of PEGDA prepolymer

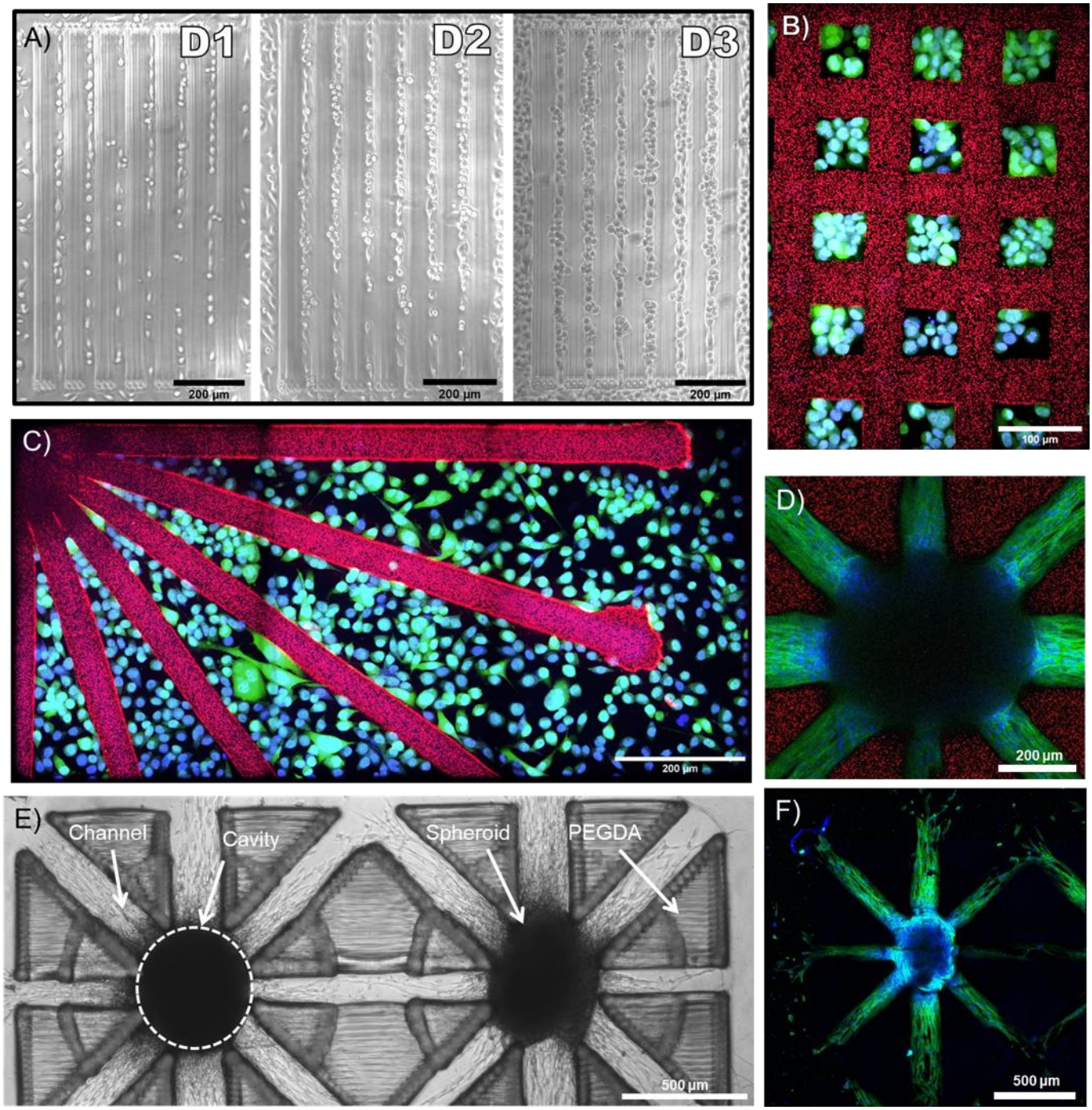

Figure 9. Illustration of cell and spheroid patterning on PEGDA patterns . (A, B, C) PC3 cells were cultivated on non-adherent PEGDA arrays of lines. (A) Images show a time lapse taken at day 1, 2, and 3. (B,C) PC3 cells after 3 days of culture. (D-E-F) Spheroids generated from hASCs were cultivated on PEGDA channel arrays. Pictures were taken at day 3 for (D-E) and day 6 for (F). (A-E) are bright field images and (B, C, D, F) are confocal images (PEGDA structures can be seen with mCherry nanoparticles (B, C, D), actin is marked in green (B, C, D, F), and nuclei are marked in blue (B, C, D, F)).

containing suspensions of fluorescent nanoparticles. Even in the case of enclosed structures, such as those presented in figure 8.B., we did not observe any impact of the presence of polymerized structures in the exposure area prior to the injection of a second material. The structures show a homogeneous shape, composition, and constant resolution (line width of 50 µm). Similar results were obtained in the case of 3D multilayer structures, such as the helicoïdal structure shown in figure 8.C. That structure was obtained using three standard PEGDA solutions (1st with green particles, 2nd with red particles, and 3rd without nanoparticles). This millimeter-scale structure was obtained by stacking five layers with a thickness of 100 µm. For each layer, the systems performed successive injections of materials with φ_{in} = 30 µL/min, Rφ = 5, and a flushing time of 90 s. Fluorescence imaging confirmed the stability of the printing process. These results also show that, for these conditions, there is no cross-contamination of materials in the printed features, which would indicate insufficient material inflow or flushing time when switching from one material to another. Han et al. achieved a switching time at 90% of 8 s [20]. However, they impose major stress on the printing structures with flowrates of approximately 1 mL/s, which is around 300-times the flowrate we used in this work. A compromise might be determined by the user to balance the advantages of fast switching time and high flowrate.

3.5 Printing scaffolds for cell patterning and spheroid engineering

We investigated how a cell colony could be patterned by non-adherent PEGDA printed on a glass surface. Cells (PC3-GFP) were seeded onto arrays of lines (Fig. 9.A), grids (Fig. 9.B), and converging lines (Fig. 9.C). As expected, no cells were detected on the PEGDA structures at day 1, confirming its protein-repellant and non-adherent properties (Fig. 9.A) while some cells can be observed even in the narrow gap separating the lines (gap = 20 µm). Cell division led to cell confluence after day 3 of culture. The 3D-FlowPrint technology allowed us to explore cell development in specific and tuned geometric conditions. Interestingly, we can see the cells starting to grow out of the PEGDA lines (height = 50 µm) at day 3. As shown in figure 9.C, cell development proceeded until an accessible distance of 10 µm between two converging lines. The 3D-FlowPrint technology could also be used to probe cell aggregates using a PEGDA grid (Fig. 9.B).

We also investigated how cell migration from human ASC spheroids can be spatially controlled using guiding structures based on differential cell adhesive properties. This printing technology allowed us to generate high-aspect-ratio non-adherent PEGDA patterns delimiting cavities (D = 450 µm, h = 600 µm) surrounded by guiding channels with different widths (100, 150, and 200 µm, Fig. 9.D-F). Cavity size was adjusted to spheroid dimension allowing hosting of the spheroids inside and maintaining them during culture. Cell attachment was observed in the adhesive areas in the first hours of culture. F-actin phalloidin staining revealed that, after 3 days, spheroid sprouting was restricted to the adhesive channels. Cell colonization was only restricted by the PEGDA geometry independently of channel size. Altogether, these results suggest that this printing approach could be adapted for further characterization of cell confinement and patterning effects on biological processes. This design may be especially useful to study the mechanisms of confined migration, known to promote cancer cell invasion [47]. Moreover, being able to drive spheroid fusion [48] or interconnectivity [49], [50] in biomaterials is currently of major interest in the tissue engineering field.

4 Conclusion

Most 3D printing methods reported so far lack the ability to print multimaterial objects in combination with high-resolution. Some have achieved this goal by laborious swapping between reservoirs or by printing inside fluidic chambers. In this article, we proposed a new method to 3D print multimaterial high-resolution objects by combining photopolymerization with a microfluidic printhead. Such a system prints directly in immersion in open media and does not require a tank of material, since the printhead is itself responsible for material supply without cross-contaminating the surrounding environment. By disassociating the polymerization process from the material supply, we were able to reach high-resolution printing (down to 10 µm in the XY plane) with multimaterial ability. Unlike most extrusion systems, the material does not need any specific properties, such as shear thinning, and can have a viscosity close to that of water. This printer also benefits from two-resolution printing to promote overall printing speed. Using a second wavelength with a dual-fiber printhead could be useful for heterogeneous structures with specific materials, as proposed by Ravanbakhsh in 2021 [6].

In this study, we 3D-printed the printhead itself to gain time, cost, and especially versatility. The printhead has been optimized through Comsol simulation by adding or removing structures at the apex in order to enhance the confinement ability and to direct the injected material toward the polymerization point. Similar simulations helped us to demonstrate our capability to confine the injected material in the enclosure below the printhead and the substrate without cross-contamination. This was achieved by choosing the right printing parameters through systematic microfluidic simulations and correlation to experiments. We demonstrated that in-flow photopolymerization was achievable, and we characterized the theoretical dose threshold. We demonstrated the potential of our system to print close, non-touching structures without the issue of dose overlapping in the gap. We presented multiple examples of objects printed with this technology, including high-resolution printing in the XYZ axis, high-aspect-ratio structures, inscribed structures, and multimaterial structures. Finally, we used the 3D-FlowPrint technology to create 2.5D objects to culture cells and spheroids on constrained environments, showing the specific development of the aforementioned elements.

In the future, enlarging the range of printable biomaterials is the main objective. For example, combining PEGDA-based materials with gelatin methacrylate (Gel-MA), methacrylated collagen (Col-MA) or methacrylated hyaluronic Acid (HA-MA) appears to be a promising perspective to promote cell adhesion [51] while keeping the hydrodynamic properties close to those of PEGDA. Materials with high contents of HA-MA or Gel-MA would allow introducing cell suspensions directly within the hydrogel formulation and thus opening a path towards 3D bioprinting. From this perspective, the multiplexing and multiresolution capacities of our approach would provide opportunities for

the creation of heterogeneous multiscale structures requiring the organization of specific cell populations in complex architectures.

Acknowledgements and funding

The authors would like to acknowledge Manon Naudé and Marie-Charline Blatché (LAAS-CNRS, Toulouse, FRANCE) for their support in cell culture experiments, Laurence Vaysse and Louis Casteilla (Restore, UMR 1301 (Inserm) / UMR 5070 (CNRS), Toulouse, FRANCE) for their support in the analysis of biological results, Brice Ronsin (CBD Imaging core facility, TRI Genotoul, Toulouse France) for his support in confocal imaging. This work was supported by the French RENATECH network. It was partly supported as part of the MultiFAB project funded by FEDER European Regional Funds and French Région Occitanie (16007407/MP0011594), by the HoliFAB project funded by the European Union's H2020 program (760927), by the French national agency for the research (ANR Printiss, ANR21CE1941), and by the French national agency of research and technology (2020/0037).

Declaration of conflicts of interest

Victor Fournie and Arnaud Reitz are employees of Fluigent SA (Kremlin-bicètre, 94270, FRANCE). The remaining authors have no conflicts of interest to declare. L. Malaquin, S. Assie-Souleille and V. Fournie (among other inventors) have patented the 3D-FlowPrint technology (EP3661754 - 2020-06-10).

References

[1] A. C. Daly, M. E. Prendergast, A. J. Hughes, et J. A. Burdick, « Bioprinting for the Biologist », *Cell*, vol. 184, n° 1, p. 18‑ 32, janv. 2021, doi: 10.1016/j.cell.2020.12.002.

[2] S. V. Murphy et A. Atala, « 3D bioprinting of tissues and organs », *Nature Biotechnology 2014 32:8*, vol. 32, n° 8, p. 773‑ 785, août 2014, doi: 10.1038/nbt.2958.

[3] P. Bajaj, R. M. Schweller, A. Khademhosseini, J. L. West, et R. Bashir, « 3D Biofabrication Strategies for Tissue Engineering and Regenerative Medicine », 2014, doi: 10.1146/annurev-bioeng-071813-105155.

[4] I. T. Ozbolat et M. Hospodiuk, « Current advances and future perspectives in extrusion-based bioprinting », *Biomaterials*, vol. 76, p. 321‑ 343, janv. 2016, doi: 10.1016/j.biomaterials.2015.10.076.

[5] H. Gudapati, M. Dey, et I. Ozbolat, « A comprehensive review on droplet-based bioprinting: Past, present and future », *Biomaterials*, vol. 102, p. 20‑ 42, sept. 2016, doi: 10.1016/J.BIOMATERIALS.2016.06.012.

[6] H. Ravanbakhsh, V. Karamzadeh, G. Bao, L. Mongeau, D. Juncker, et Y. S. Zhang, « Emerging Technologies in Multi-Material Bioprinting », *Advanced Materials*, vol. 33, n° 49, p. 2104730, 2021, doi: 10.1002/adma.202104730.

[7] L. Ning et X. Chen, « A brief review of extrusion-based tissue scaffold bio-printing », *Biotechnology Journal*, vol. 12, n° 8, p. 1600671‑ 1600671, août 2017, doi: 10.1002/BIOT.201600671.

[8] R. Devillard *et al.*, « Chapter 9 - Cell Patterning by Laser-Assisted Bioprinting », in *Methods in Cell Biology*, vol. 119, M. Piel et M. Théry, Éd. Academic Press, 2014, p. 159‑ 174. doi: 10.1016/B978-0-12-416742-1.00009-3.

[9] D. Hakobyan *et al.*, « Laser-Assisted Bioprinting for Bone Repair », in *3D Bioprinting: Principles and Protocols*, J. M. Crook, Éd. New York, NY: Springer US, 2020, p. 135‑ 144. doi: 10.1007/978-1-0716-0520-2_8.

[10] Z. Zheng, D. Eglin, M. Alini, G. R. Richards, L. Qin, et Y. Lai, « Visible Light-Induced 3D Bioprinting Technologies and Corresponding Bioink Materials for Tissue Engineering: A Review », *Engineering*, vol. 7, n° 7, p. 966‑ 978, juill. 2021, doi: 10.1016/j.eng.2020.05.021.

[11] T. Zandrini, S. Florczak, R. Levato, et A. Ovsianikov, « Breaking the resolution limits of 3D bioprinting: future opportunities and present challenges », *Trends in Biotechnology*, déc. 2022, doi: 10.1016/j.tibtech.2022.10.009.

[12] Q. Ge *et al.*, « Projection micro stereolithography based 3D printing and its applications », *Int. J. Extrem. Manuf.*, vol. 2, n° 2, p. 022004, juin 2020, doi: 10.1088/2631-7990/ab8d9a.

[13] H. Kumar et K. Kim, « Stereolithography 3D Bioprinting », *Methods in Molecular Biology*, vol. 2140, p. 93‑ 108, 2020, doi: 10.1007/978-1-0716-0520-2_6/COVER.

[14] L. Yang, F. Mayer, U. H. F. Bunz, E. Blasco, et M. Wegener, « Multi-material multi-photon 3D laser micro- and nanoprinting », *gxjzz*, vol. 2, n° 3, p. 296‑ 312, sept. 2021, doi: 10.37188/lam.2021.017.

[15] C. Zhou, Y. Chen, Z. Yang, et B. Khoshnevis, « Digital material fabrication using mask-image-projection-based stereolithography », *Rapid Prototyping Journal*, vol. 19, n° 3, p. 153‑ 165, 2013, doi: 10.1108/13552541311312148/FULL/XML.

[16] Y. Lu *et al.*, « Microstereolithography and characterization of poly(propylene fumarate)-based drug-loaded microneedle arrays », *Biofabrication*, vol. 7, n° 4, p. 045001, sept. 2015, doi: 10.1088/1758-5090/7/4/045001.

[17] Z.-C. Ma *et al.*, « Femtosecond laser programmed artificial musculoskeletal systems », *Nat Commun*, vol. 11, n° 1, Art. n° 1, sept. 2020, doi: 10.1038/s41467-020-18117-0.

[18] B. Grigoryan *et al.*, « Development, characterization, and applications of multi-material stereolithography bioprinting », *Scientific Reports* |, vol. 11, p. 3171‑ 3171, 123apr. J.-C., doi: 10.1038/s41598-021-82102-w.

[19] A. K. Miri *et al.*, « Microfluidics-Enabled Multimaterial Maskless Stereolithographic Bioprinting », *Advanced Materials*, vol. 30, n° 27, p. 1800242, 2018, doi: 10.1002/adma.201800242.

[20] D. Han, C. Yang, N. X. Fang, et H. Lee, « Rapid multi-material 3D printing with projection micro-stereolithography using dynamic fluidic control », *Additive Manufacturing*, vol. 27, p. 606‑ 615, mai 2019, doi: 10.1016/J.ADDMA.2019.03.031.
[21] F. Mayer, S. Richter, J. Westhauser, E. Blasco, C. Barner-Kowollik, et M. Wegener, « Multimaterial 3D laser microprinting using an integrated microfluidic system », *Science Advances*, vol. 5, n° 2, févr. 2019, doi: 10.1126/SCIADV.AAU9160/SUPPL_FILE/AAU9160_SM.PDF.
[22] G. Lipkowitz *et al.*, « Injection continuous liquid interface production of 3D objects », *Science Advances*, vol. 8, n° 39, p. eabq3917, sept. 2022, doi: 10.1126/sciadv.abq3917.
[23] M. A. Skylar-Scott, J. Mueller, C. W. Visser, et J. A. Lewis, « Voxelated soft matter via multimaterial multinozzle 3D printing », *Nature 2019 575:7782*, vol. 575, n° 7782, p. 330‑ 335, nov. 2019, doi: 10.1038/s41586-019-1736-8.
[24] D. Dendukuri, D. C. Pregibon, J. Collins, T. A. Hatton, et P. S. Doyle, « Continuous-flow lithography for high-throughput microparticle synthesis », *Nature Mater*, vol. 5, n° 5, Art. n° 5, mai 2006, doi: 10.1038/nmat1617.
[25] S. C. Laza, M. Polo, A. A. R. Neves, R. Cingolani, A. Camposeo, et D. Pisignano, « Two-Photon Continuous Flow Lithography », *Adv. Mater.*, vol. 24, n° 10, p. 1304‑ 1308, mars 2012, doi: 10.1002/adma.201103357.
[26] L. Malaquin, J. L. Viovy, S. Assie-Souleille, X. Dollat, et V. Fournie, « Tête d'impression d'une imprimante, imprimante et procédé d'impression », EP3661754A1, 10 juin 2020 Consulté le: 6 janvier 2023. [En ligne]. Disponible sur: https://patents.google.com/patent/EP3661754A1/fr?oq=EP3661754
[27] D. Juncker, M. Qasaimeh, A. Mckinney, et A. Hur Queval, « Multipurpose microfluidic probe Related papers Microfluidics for Processing Surfaces and Miniat urizing Biological Assays Chamber and microfluidic probe for microperfusion of organot ypic brain slices », 2005, doi: 10.1038/nmat1435.
[28] M. A. Qasaimeh, T. Gervais, et D. Juncker, « Microfluidic quadrupole and floating concentration gradient », *Nature Communications 2011 2:1*, vol. 2, n° 1, p. 1‑ 8, sept. 2011, doi: 10.1038/ncomms1471.
[29] A. Brimmo, P.-A. Goyette, R. Alnemari, T. Gervais, et M. A. Qasaimeh, « 3D Printed Microfluidic Probes », *Sci Rep*, vol. 8, n° 1, Art. n° 1, juill. 2018, doi: 10.1038/s41598-018-29304-x.
[30] K. S. Lim *et al.*, « New Visible-Light Photoinitiating System for Improved Print Fidelity in Gelatin-Based Bioinks », 2016, doi: 10.1021/acsbiomaterials.6b00149.
[31] J. M. Vuksanović, M. L. Kijevčanin, et I. R. Radović, « Poly(ethylene glycol) diacrylate as a novel chaotropic compound for design of aqueous biphasic systems », *Journal of Molecular Liquids*, vol. 261, p. 250‑ 264, juill. 2018, doi: 10.1016/J.MOLLIQ.2018.04.023.
[32] S. Muller *et al.*, « Human adipose stromal-vascular fraction self-organizes to form vascularized adipose tissue in 3D cultures », *Sci Rep*, vol. 9, n° 1, Art. n° 1, mai 2019, doi: 10.1038/s41598-019-43624-6.
[33] C. A. Schneider, W. S. Rasband, et K. W. Eliceiri, « NIH Image to ImageJ: 25 years of image analysis », *Nature Methods 2012 9:7*, vol. 9, n° 7, p. 671‑ 675, juin 2012, doi: 10.1038/nmeth.2089.
[34] E. H. W. Meijering, W. J. Niessen, et M. A. Viergever, « Quantitative evaluation of convolution-based methods for medical image interpolation », *Medical Image Analysis*, vol. 5, n° 2, p. 111‑ 126, juin 2001, doi: 10.1016/S1361-8415(00)00040-2.
[35] P. Juskova, A. Ollitrault, M. Serra, J. L. Viovy, et L. Malaquin, « Resolution improvement of 3D stereo-lithography through the direct laser trajectory programming: Application to microfluidic deterministic lateral displacement device », *Analytica Chimica Acta*, vol. 1000, p. 239‑ 247, févr. 2018, doi: 10.1016/J.ACA.2017.11.062.
[36] M. Babi *et al.*, « Tuning the Nanotopography and Chemical Functionality of 3D Printed Scaffolds through Cellulose Nanocrystal Coatings », *ACS Appl. Bio Mater.*, vol. 4, n° 12, p. 8443‑ 8455, déc. 2021, doi: 10.1021/acsabm.1c00970.
[37] N. Paxton, W. Smolan, T. Böck, F. Melchels, J. Groll, et T. Jungst, « Proposal to assess printability of bioinks for extrusion-based bioprinting and evaluation of rheological properties governing bioprintability », *Biofabrication*, vol. 9, n° 4, p. 044107, nov. 2017, doi: 10.1088/1758-5090/aa8dd8.
[38] Y. Guo, H. S. Patanwala, B. Bognet, et A. W. K. Ma, « Inkjet and inkjet-based 3D printing: connecting fluid properties and printing performance », *Rapid Prototyping Journal*, vol. 23, n° 3, p. 562‑ 576, janv. 2017, doi: 10.1108/RPJ-05-2016-0076.
[39] H. Lin *et al.*, « Application of visible light-based projection stereolithography for live cell-scaffold fabrication with designed architecture », *Biomaterials*, vol. 34, n° 2, p. 331‑ 339, janv. 2013, doi: 10.1016/j.biomaterials.2012.09.048.
[40] J. P. Mazzoccoli, « Properties of Poly(ethylene glycol) Diacrylate Blends and Acoustically Focused Multilayered Biocomposites Developed for Tissue Engineering Applications », 2008.
[41] B. D. Fairbanks, M. P. Schwartz, C. N. Bowman, et K. S. Anseth, « Photoinitiated polymerization of PEG-diacrylate with lithium phenyl-2,4,6-trimethylbenzoylphosphinate: polymerization rate and cytocompatibility », *Biomaterials*, vol. 30, n° 35, p. 6702‑ 6707, déc. 2009, doi: 10.1016/J.BIOMATERIALS.2009.08.055.
[42] E. Mancha Sánchez *et al.*, « Hydrogels for Bioprinting: A Systematic Review of Hydrogels Synthesis, Bioprinting Parameters, and Bioprinted Structures Behavior », *Frontiers in Bioengineering and Biotechnology*, vol. 8, 2020, doi: 10.3389/FBIOE.2020.00776/BIBTEX.
[43] D. Dendukuri et P. S. Doyle, « The Synthesis and Assembly of Polymeric Microparticles Using Microfluidics », *Advanced Materials*, vol. 21, n° 41, p. 4071‑ 4086, 2009, doi: 10.1002/adma.200803386.
[44] M. Ziauddin, A.-H. Mourad, et S. Khashan, « Maskless Lithography Using Negative Photoresist Material: Impact of UV Laser Intensity on the Cured Line Width », *Lasers in Manufacturing and Materials Processing*, vol. 5, p. 1‑ 10, juin 2018, doi: 10.1007/s40516-018-0058-2.

[45] T. Pelras, S. Glass, T. Scherzer, C. Elsner, A. Schulze, et B. Abel, « Transparent Low Molecular Weight Poly(Ethylene Glycol) Diacrylate-Based Hydrogels as Film Media for Photoswitchable Drugs », *Polymers 2017, Vol. 9, Page 639*, vol. 9, n° 12, p. 639‑ 639, nov. 2017, doi: 10.3390/POLYM9120639.
[46] L. Flach et R. P. Chartoff, « A process model for nonisothermal photopolymerization with a laser light source. I: Basic model development », *Polymer Engineering & Science*, vol. 35, n° 6, p. 483‑ 492, 1995, doi: 10.1002/pen.760350605.
[47] D. Fanfone *et al.*, « Confined migration promotes cancer metastasis through resistance to anoikis and increased invasiveness », *eLife*, vol. 11, p. e73150, mars 2022, doi: 10.7554/eLife.73150.
[48] A. C. Daly, M. D. Davidson, et J. A. Burdick, « 3D bioprinting of high cell-density heterogeneous tissue models through spheroid fusion within self-healing hydrogels », *Nat Commun*, vol. 12, n° 1, Art. n° 1, févr. 2021, doi: 10.1038/s41467-021-21029-2.
[49] J. J. Kim, M. Jorfi, R. E. Tanzi, D. Y. Kim, P. S. Doyle, et D. Irimia, « Patterning of interconnected human brain spheroids », *Lab Chip*, vol. 21, n° 18, p. 3532‑ 3540, sept. 2021, doi: 10.1039/d0lc01112f.
[50] S. Kim *et al.*, « Spatially arranged encapsulation of stem cell spheroids within hydrogels for the regulation of spheroid fusion and cell migration », *Acta Biomaterialia*, vol. 142, p. 60‑ 72, avr. 2022, doi: 10.1016/j.actbio.2022.01.047.
[51] X. Zhan, « Effect of matrix stiffness and adhesion ligand density on chondrogenic differentiation of mesenchymal stem cells », *Journal of Biomedical Materials Research Part A*, vol. 108, n° 3, p. 675‑ 683, mars 2020, doi: 10.1002/JBM.A.36847.

Supplementary Data

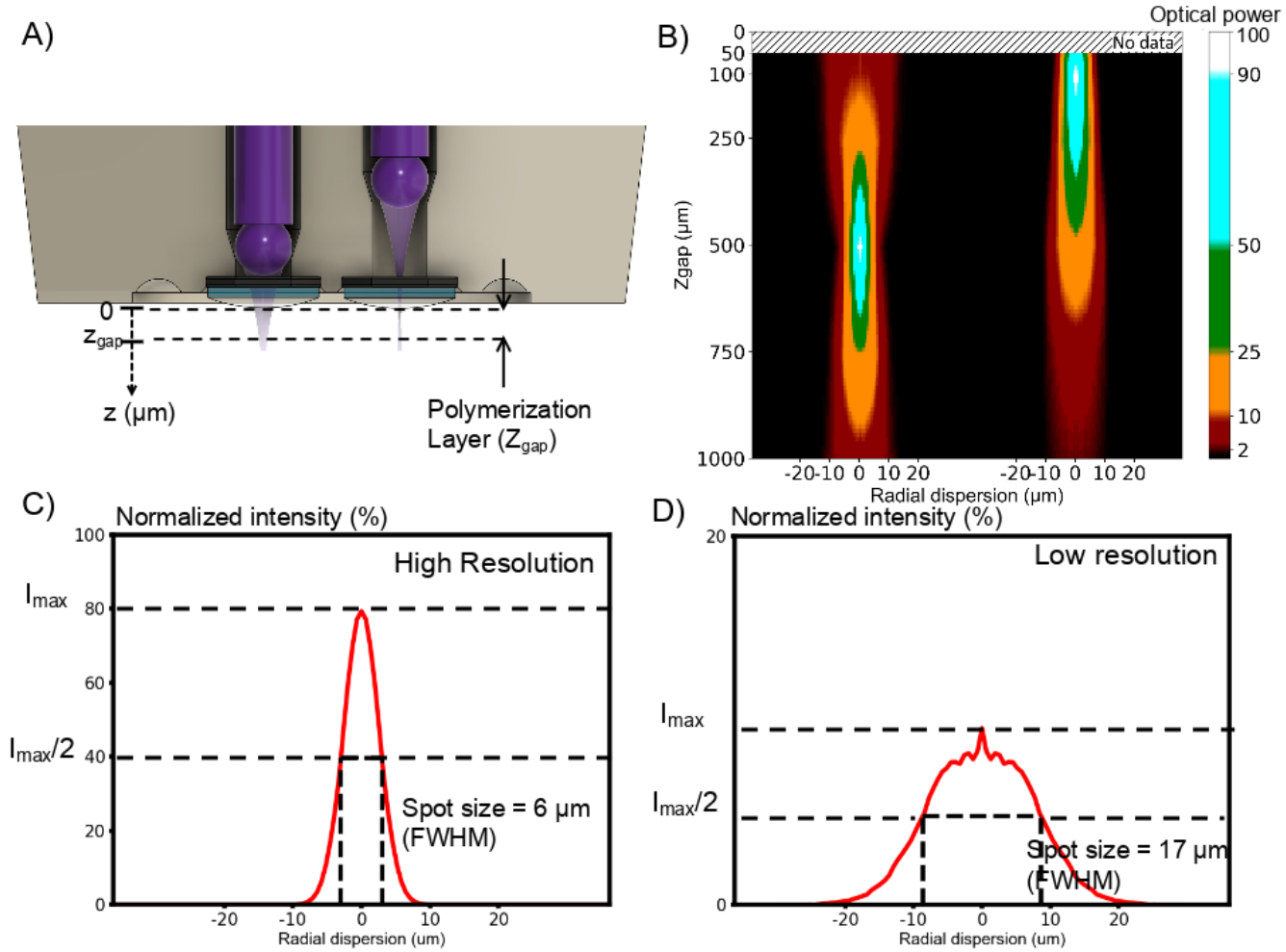

Supplementary Figure 1. Two optical configurations were obtained by adjusting the working distance between the lensed ball fibers and the printhead surface. (A) Schematic cross-section of a printing head with two inserted shifted optical fibers, blocked at 0 µm and 600 µm. (B) Radial dispersion of the laser intensity for increasing Z_{gap}. (C-D) Radial profiles of the laser beam for Z_{gap} = 50 µm.

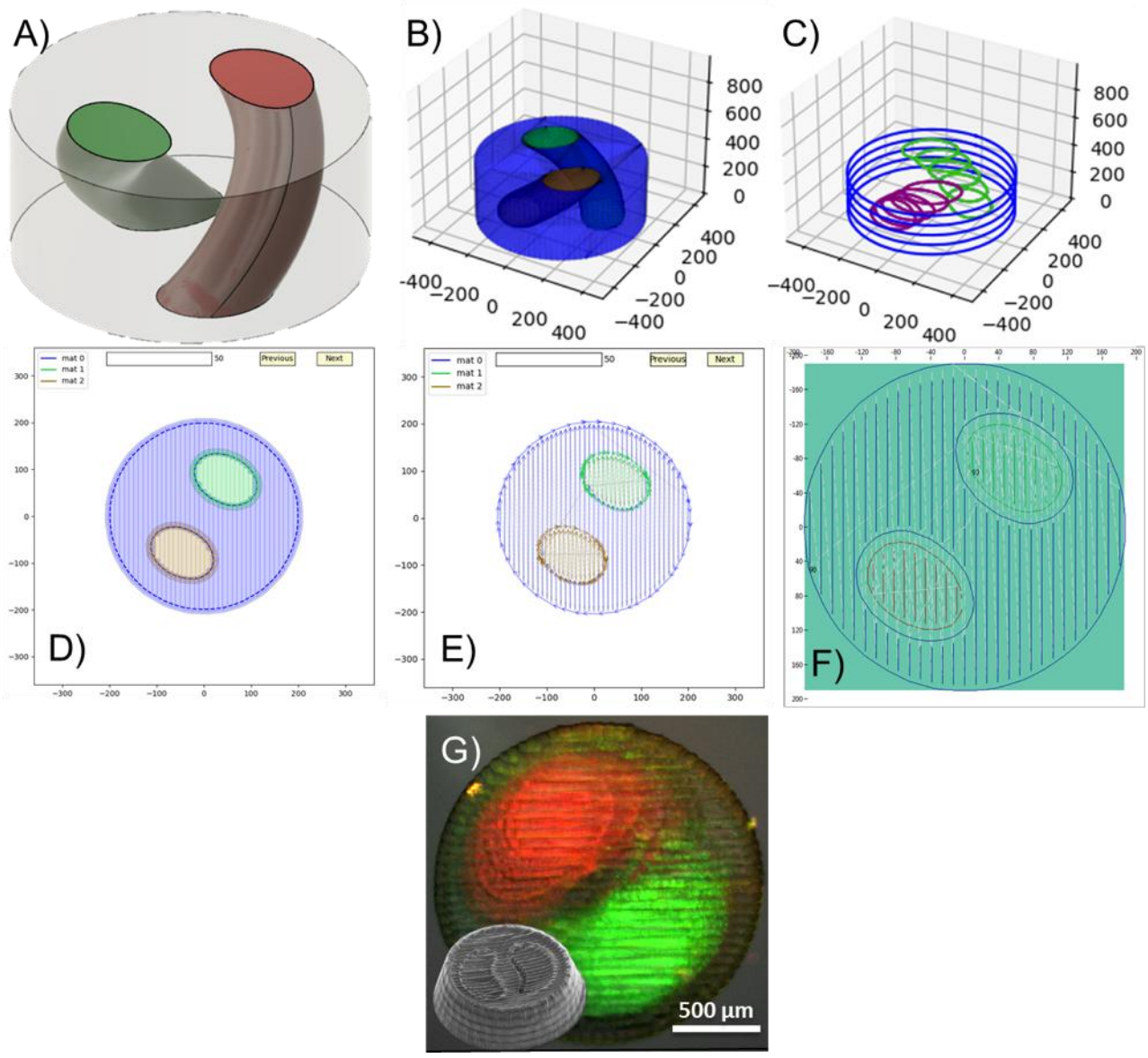

Supplementary Figure 2. Workflow process for the digitalization of a 3D object. (A) 3D picture of CAD objects saved as STL. (B) Image of the STL files imported in python software. Image of the object after slicing (C), vectorization (D), and ordering for saving in Gcode (E). (F) Picture of the same slice of the Gcode read by the experimental software (LABView). (G) Fluorescent and SEM pictures of the printed objects.

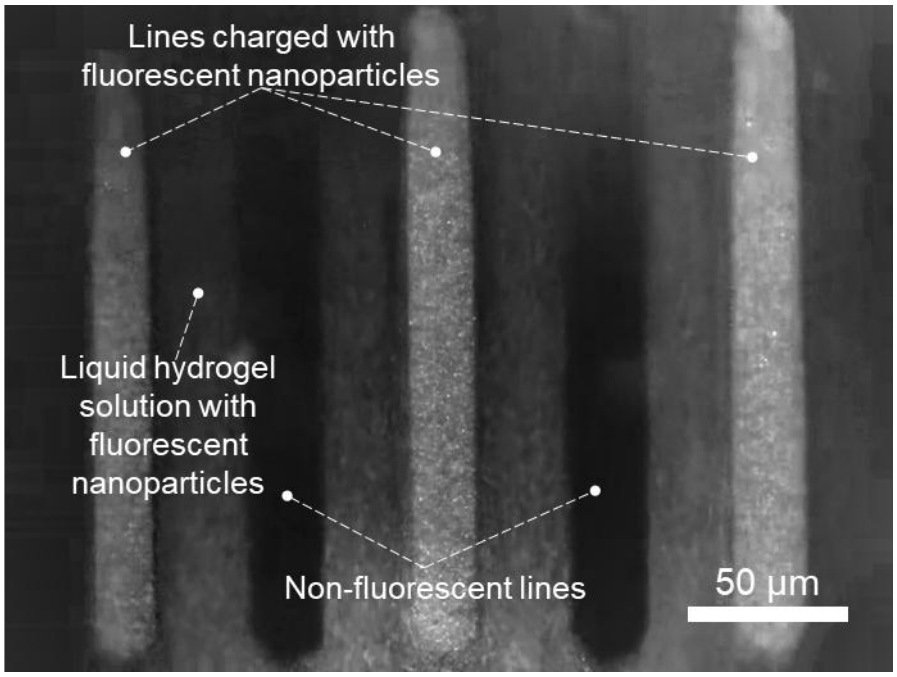

Supplementary Figure 3. Optical image of 5 printed lines. The 1st, 3rd, and 5th contain nanoparticles visible under fluorescence, unlike lines 2 and 4. This picture was taken after printing but before rinsing, so we can see the nanoparticle-charged hydrogel material around the lines, which allows us to see the non-fluorescent lines by contrast. The printing video is available online.

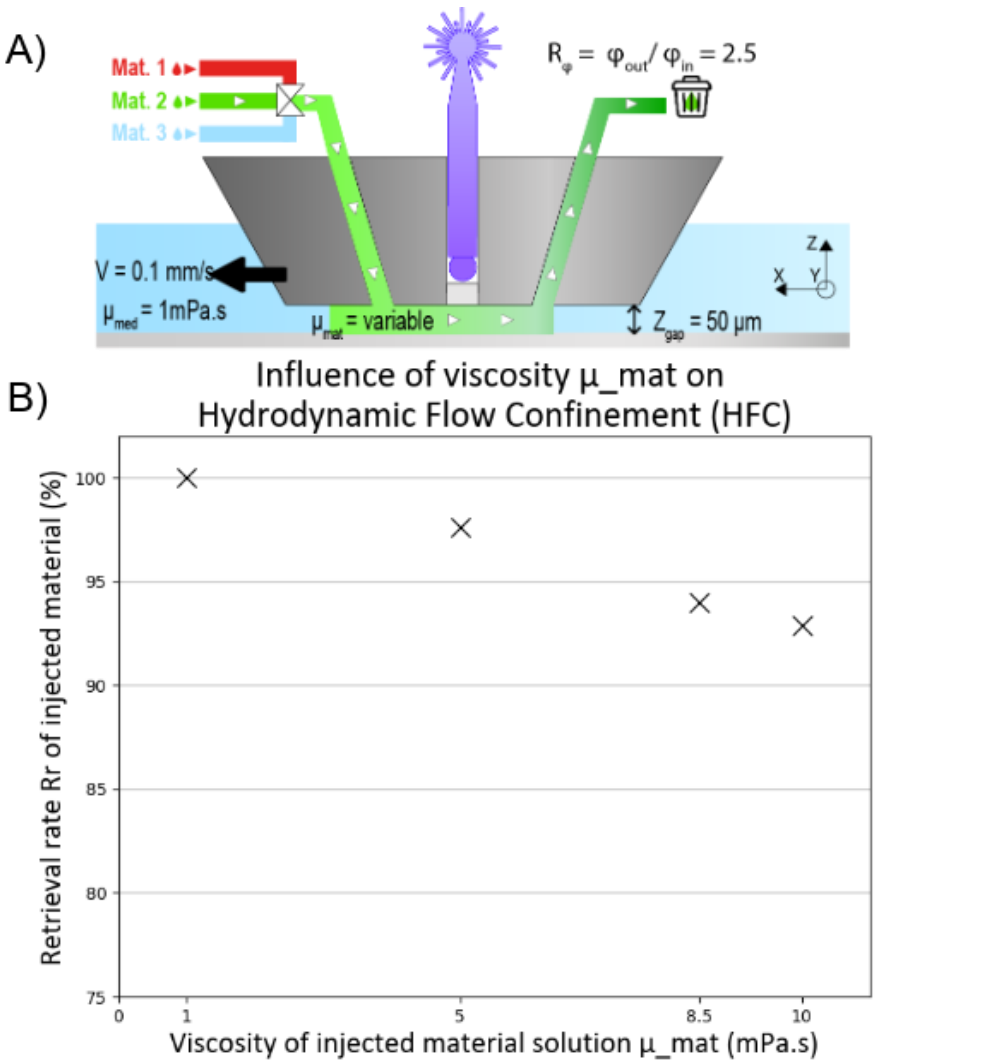

Supplementary Figure 4. Influence of the injected material viscosity on the hydrodynamic confinement (A) Cross-section schematic of the printhead showing the main parameters of the study. (B) Results of Comsol simulations showing the influence of the viscosity of the injected material (μ_{mat}) on the hydrodynamics in the 1 to 10 mPa.s range. V = 0.1 mm/s, Z_{gap} = 50 µm, Rφ = 2.5, φin = 25 µL/min, μ_{med} = 1 mPa.s. Black crosses are simulation points.

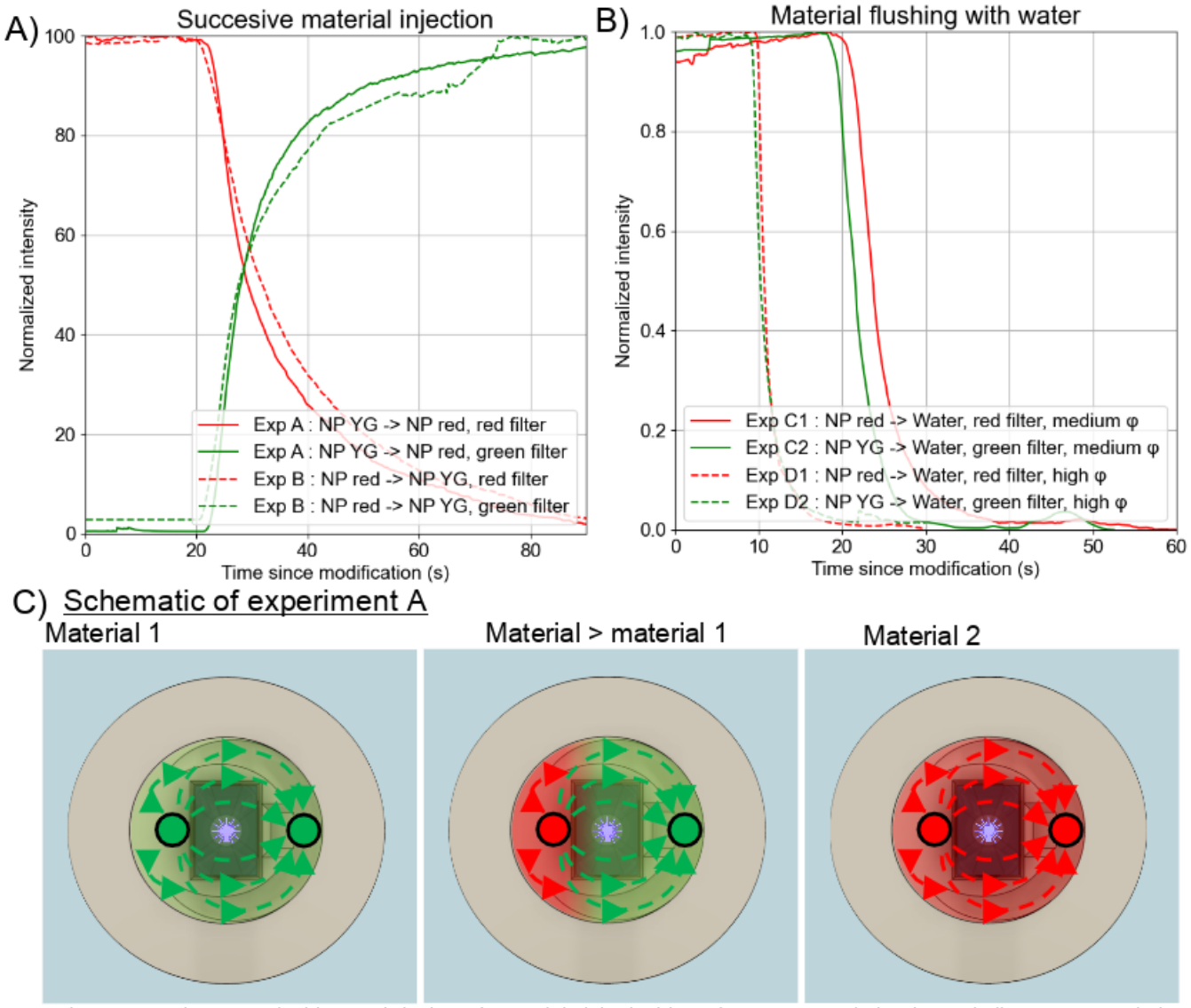

Supplementary Figure 5. Flushing and rinsing of material. (A) Flushing of a PEGDA solution by a similar PEGDA solution with different nanoparticles. Experiment A shows a material with red nanoparticles flushing a material with yellow-green nanoparticles, while experiment B shows the opposite. φ_{in} = 30 µL/min, Rφ = 5. (B) Rinsing of a PEGDA material with DI-water at different flowrates while keeping Rφ = 5. Medium flowrates: φ_{in} = 30 µL/min, high flowrates: φ_{in} = 60 µL/min. (A-B) Command to change materials at time = 0 s. PEGDA solution = [40% PEGDA 700, 60% water DI, 0.01% mCherry or GFP nanoparticles]. The printhead is not moving (V = 0 mm/s, Z_{gap} = 100 µm). Curves obtained by measuring the fluorescence of nanoparticles over time with a green or red filter. (C) Schematic of experiment A, view below the printing head.

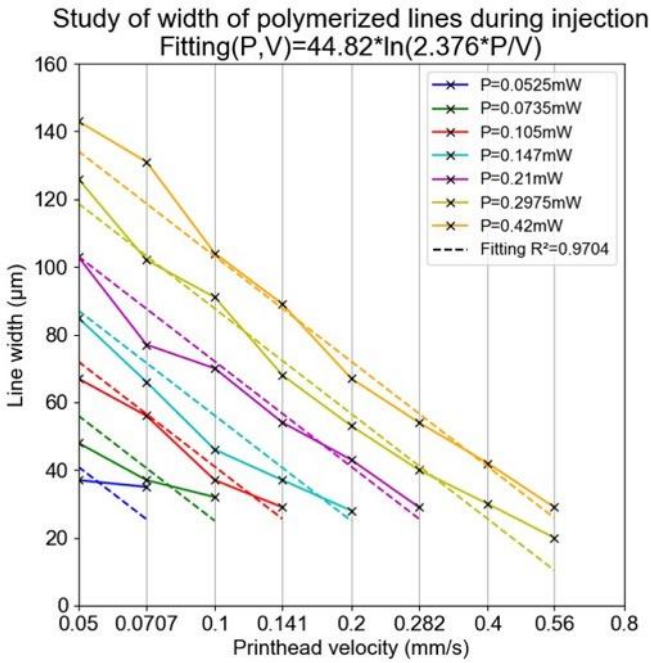

*Supplementary Figure 6. Experimental results for the influence of the input power and printhead velocity on the printing line width. h = 75 µm, φ_{in} = 25 µL/min and Rφ = 5. Fitting realized with eq. 3: Width(Pout,V)=k1*ln(k2*Pout/V), with k_1 = 44.82, k_2 = 2.376.*

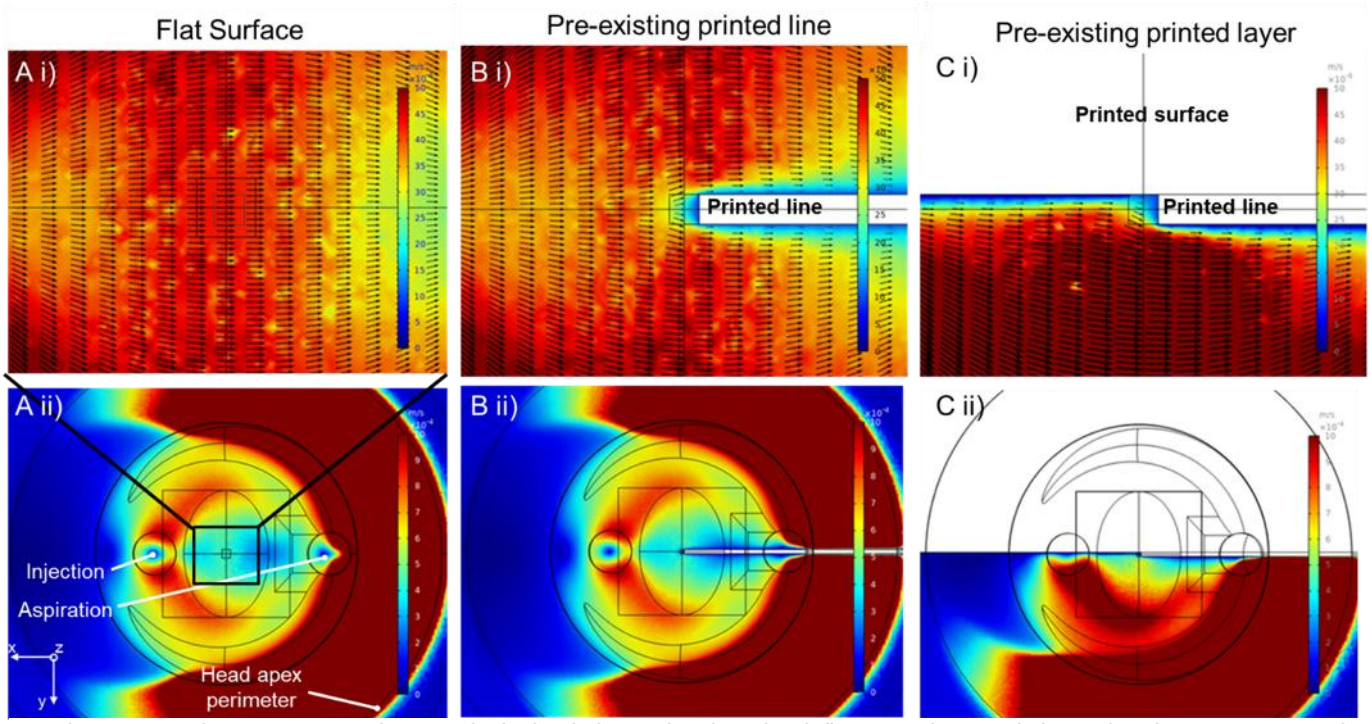

Supplementary Figure 7. Comsol Numerical simulations showing the influence of pre-existing printed structures on the hydrodynamic flow. (A) Reference. (B) Pre-existing printed line. (C) Pre-existing printed surface. (A-B-C) Z_{gap} = 50 µm, φ_{in} = 25 µL/min, Rφ = 5. μ_{med} = 1 mPa.s. μ_{mat} = 8.5 mPa.s. Outer boundaries, support, and printed structures were implemented with a velocity boundary slip condition to represent the printhead motion at V = 0.1 mm/s. Color scales represent the velocities of the material around the polymerization area (i, maximum = 0.5 mm/s) or on the scale of the printhead (ii, maximum = 1 mm/s)). Black arrows represent the direction and the magnitude of the fluid velocity. The color cross-sections and the arrows are at mid-height or Z_{gap} = 25 µm. In white, previously printed structures are modifying the flow repartition and decreasing the material velocity in their vicinity.

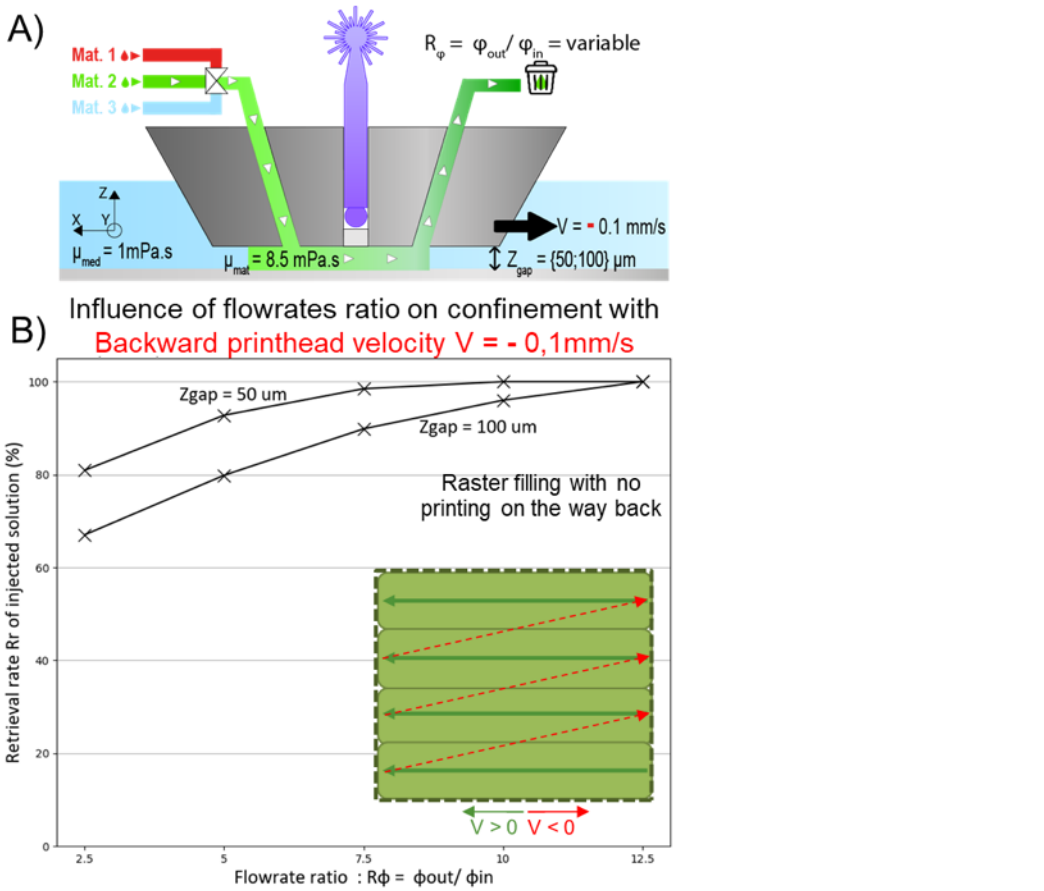

Supplementary Figure 8. Evolution of the material retrieval rate as a function of flowrate ratio in raster writing mode. (A) Cross-sectional schematic of the printhead showing the main parameters of the study. (B) Results of Comsol simulations showing the influence of flowrate ratio on the retrieval rate for negative speed. V = -0.1 mm/s. Z_{gap} = {50; 100} µm, μ_{mat} = 1 mPa.s, μ_{med} = 8.5 mPa.s. Black crosses are simulation points. Due to the higher Rφ needed to keep HFC with backward motion, the laser was turned on for positive velocities only. The printing protocol was as follows: i) print first line in the positive direction with Rφ = 5, ii) then change to Rφ = 10, iii) go back to the beginning of the next line, and iv) change back to Rφ = 5 to limit material waste.